Atmos. Chem. Phys., 25, 6121–6139, 2025
https://doi.org/10.5194/acp-25-6121-2025

Atmospheric Chemistry and Physics
Open Access

Cold pools mediate mesoscale adjustments of trade-cumulus fields to changes in cloud droplet number concentration

Pouriya Alinaghi, Fredrik Jansson, Daniel A. Blázquez, and Franziska Glassmeier

Department of Geoscience & Remote Sensing, Delft University of Technology, Delft, the Netherlands

Correspondence: Pouriya Alinaghi (p.alinaghi@tudelft.nl)

Received: 8 November 2024 – Discussion started: 20 November 2024
Revised: 21 March 2025 – Accepted: 28 March 2025 – Published: 20 June 2025

Abstract. The mesoscale self-organization of trade-cumulus cloud fields is a major cloud–climate uncertainty. Cold pools, i.e., pockets of cold, dense air resulting from rain evaporation, are a key mechanism in shaping these dynamics and are controlled by the large-scale forcing. We study the microphysical sensitivity of cloud-field self-organization through cold pools by varying the cloud droplet number concentration (N_c) from 20 to $1000\,\mathrm{cm}^{-3}$ in large-eddy simulations on large $154\,\mathrm{km} \times 154\,\mathrm{km}$ domains. We find that cold pools exhibit two distinct regimes of mesoscale self-organization. Under very low N_c conditions, cold pools transition from a stage in which they are small and randomly distributed to forming large, long-lived structures that perpetuate due to the collisions of cold pools at their fronts. Under high-N_c conditions, cold pools display strongly intermittent behavior and interact with clouds through small, short-lived structures. Thus, although N_c influences the number of cold pools and, in turn, mesoscale organization, cloud depth, and cloud albedo, we find its effect on cloud cover to be minimal. Comparing the microphysical sensitivity of cold-pool-mediated mesoscale dynamics to the external, large-scale forcing shows that N_c is as important as horizontal wind and large-scale subsidence for trade-cumulus albedo. Our results highlight that cold pools mediate the adjustments of trade-cumulus cloud fields to changes in N_c. Such mesoscale adjustments need to be considered if we are to better constrain the effective aerosol forcing and cloud feedback in the trade-wind regime.

1 Introduction

Clouds play a crucial role in the climate system by modulating the Earth's energy budget through their interactions with radiation. Their net effect is to cool the planet by reflecting incoming solar radiation back into space (Stephens et al., 2012). Clouds are one of the most important sources of uncertainty in climate projections. Firstly, the cloud feedback is the most uncertain feedback to the anthropogenic forcing of the climate system, which is mainly due to the uncertain response of shallow clouds to climate change (Schneider et al., 2017; Nuijens and Siebesma, 2019; IPCC AR6, 2023). Secondly, the complex interactions between clouds and aerosols lead to the process uncertainty that makes the effective radiative forcing due to aerosol–cloud interactions the most uncertain forcing in the climate system (IPCC AR6, 2023; Bellouin et al., 2020).

Aerosol perturbations change the concentration of cloud condensation nuclei and, in turn, cloud droplet number concentration (N_c) values. Assuming a fixed cloud liquid water path, increased N_c results in a larger number of smaller cloud droplets, leading to a larger surface area to interact with radiation, and in turn increased cloud optical depth and cloud albedo, known as the *Twomey* effect (Twomey, 1977). In addition to this quasi-immediate effect that can be considered to occur on the spatiotemporal scales of individual cloud parcels, changes in N_c can also propagate to larger scales. On the single-cloud scale, increased N_c reduces the efficiency of collision–coalescence processes through smaller radii, decreasing the rain-formation efficiency, thereby delaying precipitation formation, known as the *Albrecht* or *lifetime* effect (Albrecht, 1989). This delay in precipitation formation allows clouds to live longer; get deeper; and, in the end, precipitate more intensely. Such effects can lead to an internal reorganization on the cloud-field scale, or mesoscale, which ranges from tens to hundreds of kilometers and evolves on timescales of hours to days. These effects can be considered a form of self-organization because they are not prescribed by a large-scale forcing. In addition to delayed precipitation formation, increased N_c has also been described to affect entrainment rates with effects on meso-timescales (Glassmeier et al., 2021).

For trade-cumulus cloud fields, large-eddy simulations (LESs) were first employed on small domains (6.4 km × 6.4 km to 12.8 km × 12.8 km) to investigate the response of shallow cumuli to aerosol perturbations (Xue et al., 2008; Zuidema et al., 2008). A decade later, LESs on larger domains (Seifert et al., 2015; Yamaguchi et al., 2019b) showed that the compensating internal adjusting processes, as proposed by Stevens and Feingold (2009), occur on the scales of 50 km × 50 km cumulus cloud fields, which is far beyond the scale of an individual cloud. While not their focus, these studies give a clear indication of cold-pool activity. Cold pools are pockets of cold, dense air resulting from downdrafts associated with rain evaporation. When these downdrafts reach the surface, cold pools spread outward in a circular pattern. Studies across various regimes – stratocumulus, shallow, and deep convection – indicate that cold-pool boundaries feature strong, moist updrafts, which trigger cloud formation along their edges, forming cloud rings that are often visible in satellite imagery (Xue et al., 2008; Savic-Jovcic and Stevens, 2008; Zuidema et al., 2012, 2017; Böing et al., 2012; Jeevanjee and Romps, 2013; Schlemmer and Hohenegger, 2014; Langhans and Romps, 2015; Torri et al., 2015; Drager and van den Heever, 2017; Haerter and Schlemmer, 2018; Helfer and Nuijens, 2021; Lochbihler et al., 2021; Vogel et al., 2021; Touzé-Peiffer et al., 2022). When cold pools form in close proximity, their boundaries can collide (Torri and Kuang, 2019), which intensifies the next convective event. Such cold-pool interactions through collisions implement self-organization, as has been conceptually modeled for both open-cell stratocumulus (Glassmeier and Feingold, 2017) and deep convective regimes (Haerter et al., 2019; Nissen and Haerter, 2021).

Shallow cumuli in the trades are frequently precipitating (Nuijens et al., 2009; Snodgrass et al., 2009; Radtke et al., 2022), leading to the frequent presence of cold pools in the trade-wind regime (Zuidema et al., 2012; Vogel et al., 2021; Touzé-Peiffer et al., 2022). The size and frequency of occurrence of cold pools covary with the mesoscale organization of trade-cumulus clouds (Vogel et al., 2021). Even under large-scale conditions that are invariant in time and space, LES studies show that trade-cumulus cold pools self-organize and, in turn, pattern trade-cumulus fields into arc-shaped structures (Seifert and Heus, 2013; Vogel et al., 2016). By generating strong, moist updrafts at their fronts, cold pools affect and interact with clouds (Zuidema et al., 2012; Li et al., 2014; Vogel et al., 2021; Alinaghi et al., 2025). Using large-domain LESs of the trade-wind regime, Alinaghi et al. (2025) recently showed that the cold-pool–cloud interaction expresses itself in the form of structures resembling shallow squall lines. Thus, cold pools are coupled to clouds through shallow circulations at the mesoscales that were frequently observed in the trades (George et al., 2023) and affect cloudiness (Vogel et al., 2022; Janssens et al., 2023; Alinaghi et al., 2025).

The mesoscale dynamics of trade cumulus are typically discussed in the context of cloud feedback. The trade-cumulus feedback has long been a large source of uncertainty in climate projections (Cesana and Del Genio, 2021; Myers et al., 2021). Trade-cumulus fields pattern into structures at the mesoscales that influence the cloud radiative effect (Bony et al., 2020; Alinaghi et al., 2024a; Denby, 2023). Therefore, it is crucial to explore processes through which these clouds organize and how these processes respond to the variations in large-scale cloud-controlling factors (CCFs). By employing a large ensemble of LESs, the *Cloud Botany* ensemble (Jansson et al., 2023a), Alinaghi et al. (2025) illustrated that cold pools in the trades are strongly controlled by the variations in the large-scale external CCFs. They particularly quantified the relative importance of CCFs with respect to each other. Additionally, diurnality in insolation, which acts as a time-varying CCF, was shown to strongly control the temporal evolution of cold pools throughout the entire Cloud Botany ensemble (Alinaghi et al., 2025).

Given the direct impact of N_c on precipitation formation, it is expected that trade-cumulus cold pools respond to variations in N_c (Fig. 1, link 1) and, thus, to feedback to cloud fields at the mesoscales (Fig. 1, link 2). Despite the previously investigated sensitivity of shallow cold pools to microphysics schemes (Li et al., 2015), the response of shallow cold pools to N_c has not been directly explored and quantified. Furthermore, it is unknown how such N_c variations change the interplay between cold pools and clouds in the trade-wind regime. This study explores this response by performing large-domain LESs in which we only vary cloud droplet number concentrations (N_c) from 20 to 1000 cm^{-3}. The newly added dimension of variability in N_c here also enables us to systematically investigate the relative importance of N_c compared to the other CCFs (Fig. 1, link 3) for cold pools and the radiative effect of clouds in the trade-wind regime (Fig. 1, link 4). Hence, our work serves as a step towards understanding the significance of the aerosol forcing in comparison to the trade-cumulus feedback and exploring the corresponding role of mesoscale dynamics.

This paper is structured as follows. Based on simulations discussed in Sect. 2, we first investigate how trade-cumulus cold pools respond to N_c variability (Fig. 1, link 1; Sect. 3.1 and 3.2) and how this response shapes the mesoscale organization of clouds (Fig. 1, link 2; Sect. 3.2). Second, we explore how the diurnal cycle in insolation, as a time-varying CCF

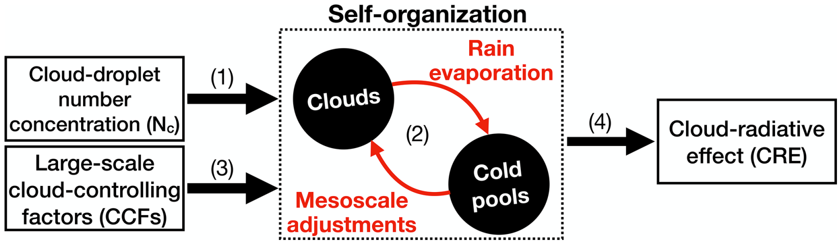

Figure 1. Conceptual picture of the study. The diagram summarizes how (link 1) cloud fields respond to changes in N_c and how (link 2) cold pools feed back to clouds (self-organization). The diagram also shows that the trade-cumulus system is forced by (link 3) the large-scale cloud-controlling factors (CCFs) whose relative importance for (link 4) the cloud radiative effect will be quantified compared to N_c.

(Fig. 1, link 3), controls the evolution and response of cold pools to N_c (Sect. 3.3). Next, we investigate the implications of our results for the cloud-field adjustments to N_c (Fig. 1, links 1 and 2; Sect. 3.4). Finally, we compare the effect of N_c on cloud-field properties and radiative effects to that of large-scale external CCFs (Fig. 1, links 3 and 4; Sect. 3.5). Conclusions are presented in Sect. 4.

2 Data and methods

We perform LESs with the Dutch Atmospheric Large-Eddy Simulation (DALES) model over domains of 153.6 km × 153.6 km, featuring a horizontal resolution of 100 m and a vertical resolution of about 20 m. All simulations are forced by the same large-scale CCFs. These follow the central reference simulation of the Cloud Botany ensemble (Jansson et al., 2023a), which corresponds to the mean large-scale conditions of the winter trades as derived from the ERA5 reanalysis data (Hersbach et al., 2020). The corresponding profiles, which are also used for initialization are shown in Fig. 2. Moreover, all simulations feature the same horizontal tendencies of cooling and drying through advection as those shown in the Cloud Botany paper (Jansson et al., 2023a, their Fig. 3). Most of the simulations feature diurnality in the solar incoming radiation, while all other CCFs are fixed in time. Thus, the variability and evolution in the simulations are driven by the interaction between the components of the system, allowing the study of processes via which the system self-organizes. For more details on the design of the Cloud Botany simulations, including the selection of parameters for the large-scale forcing, refer to Jansson et al. (2023a).

Simulations utilize the two-moment cloud microphysics scheme of Seifert and Beheng (2001) with a constant cloud droplet number concentration N_c. We conduct six 72 h simulations with varying N_c values in the set $\{20, 50, 70, 100, 200, 1000\}\,\mathrm{cm}^{-3}$. The selected range of N_c variability, from 20 to 100, is similar to that used by Seifert et al. (2015), which is based on observations of the trades (Colón-Robles et al., 2006; Gerber et al., 2008; Hudson and Noble, 2014). We also included N_c values of 200 and 1000, as recent observations from the EUREC^{4}A field campaign (Bony et al., 2017; Stevens et al., 2021) report N_c values as high as $1000\,\mathrm{cm}^{-3}$, primarily due to the presence of dust (see Fig. 9 in Quinn et al., 2021, and Figs. 9 and 10 in Bony et al., 2022). Note that, as N_c is fixed in time and space and does not evolve in our simulations, our study excludes microphysical adjustments. To gauge this limitation, we compare our results to cases from the literature with more complex microphysics.

Figure 3 visualizes that all of these simulations start from a homogeneous non-cloudy state and develop into randomly distributed cumulus clouds. Afterward, clouds self-aggregate due to the presence of self-reinforcing shallow mesoscale overturning circulations (Bretherton and Blossey, 2017; Narenpitak et al., 2021; Janssens et al., 2023). As clouds aggregate, they deepen and eventually start to precipitate, leading to the presence of mesoscale arc-like structures, indicating the presence of cold pools in the field.

Alinaghi et al. (2025) showed that the evolution of cold pools across the entire Cloud Botany ensemble is strongly controlled by the diurnality of insolation, mirroring observations of the trades (Vial et al., 2021; Vogel et al., 2021). To investigate how the evolution of cold pools is affected by variations in N_c independently of the diurnal cycle, we switch off the diurnality in insolation. To this end, we rerun simulations with N_c values of 20, 70, and $1000\,\mathrm{cm}^{-3}$, while keeping the solar zenith angle time-invariant, ensuring that the total incoming solar radiation over the entire 24 h period is equal to that of the simulations with the diurnal cycle (Alinaghi et al., 2025, their Sect. 3.2).

To diagnose cold pools, we use the 2D outputs of the mixed-layer height (h_{mix}), as h_{mix} has been shown to be a reliable indicator of trade-cumulus cold pools in both models (Rochetin et al., 2021) and observations (Touzé-Peiffer et al., 2022). We identify cold pools following Alinaghi et al. (2025): for each cloud field, we find the mode and the upper boundary (99th percentile) of an assumed symmetric probability density function (PDF) of h_{mix} that would have been observed in the absence of cold pools. The lower boundary of h_{mix} is calculated by first determining the difference between the upper boundary and the mode and then subtracting this difference from the mode. Cold pools are identified where

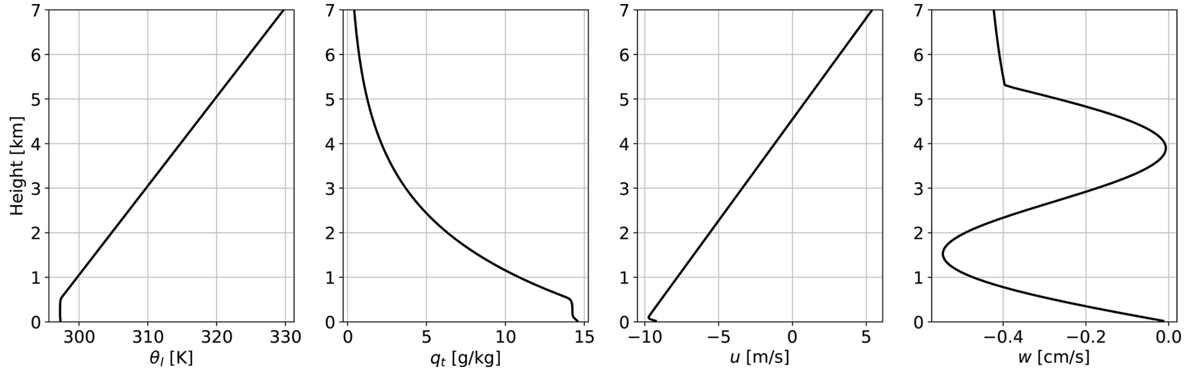

Figure 2. Large-scale and initial conditions of the simulation for potential temperature (θ_l), total moisture (q_t), horizontal wind (u), and updraft (w) following the assumptions of the Cloud Botany ensemble (Jansson et al., 2023a) with parameter values of sea-surface (potential) temperature $\theta_{l0} = 299$ K, near-surface wind speed $u_0 = -10.6\,\mathrm{m\,s^{-1}}$, moisture scale height $h_{q_t} = 1810$ m, temperature lapse rate $\Gamma = 5\,\mathrm{K\,km^{-1}}$, large-scale vertical velocity variability $w_1 = 0.0393\,\mathrm{cm\,s^{-1}}$, and horizontal wind shear $u_z = 0.0022\,(\mathrm{m\,s^{-1}})\,\mathrm{m^{-1}}$.

h_{mix} is smaller than the lower boundary of h_{mix} (see Fig. 3 in Alinaghi et al., 2025). In essence, this method identifies cold pools where h_{mix} is relatively shallower compared to other parts of the field. Alinaghi et al. (2025) showed that the response of cold pools to CCFs is not sensitive to the details of the cold-pool diagnosis performed with this method.

Using the identified cold-pool mask and a clustering method, we define cold-pool objects as 2D contiguous structures within the simulation domain at each model time step. We then quantify the number of cold pools (n_{cp}) within the domain. Additionally, we compute the domain-mean cold-pool size as follows: $s_{\mathrm{cp}} = \sum_{i=1}^{n_{\mathrm{cp}}} \sqrt{A_i}/n_{\mathrm{cp}}$, where A_i denotes the area of each cold-pool object i within the domain.

3 Results and discussion

3.1 Cloud droplet number concentration affects the spatial and temporal properties of trade-cumulus cold pools

In this section, we investigate how the spatial and temporal properties of cold pools are influenced by N_c (Fig. 1, link 1 and 2). As cold pools result from rain evaporation (Fig. 1, link 2), we first examine how clouds and rain respond to N_c in simulations without a diurnal cycle, which feature N_c values of 20, 70, and 1000 $\mathrm{cm^{-3}}$. According to theory (Albrecht, 1989) and previous LES studies (Seifert et al., 2015; Yamaguchi et al., 2019b), increased N_c reduces the efficiency of auto-conversion, delaying rain formation and allowing clouds to deepen and persist longer. Consistent with this, increased N_c leads to the accumulation of liquid water ($\mathcal{L}$; Fig. 4a), eventually resulting in the production of more intense rain ($\mathcal{R}$; Fig. 4b). Furthermore, the amplitude of fluctuations in $\mathcal{L}$ and $\mathcal{R}$ increases with increasing N_c, while their frequency decreases (Fig. 4a and b).

We quantitatively compare our results to those of Yamaguchi et al. (2019b) and Seifert et al. (2015) (Fig. 4e and f). The results of Yamaguchi et al. (2019b) were obtained on domains that were 10 times smaller but using a microphysics scheme with prescribed aerosol and prognostic cloud droplet number concentrations. The latter converges to a certain value after approximately 20 h (Yamaguchi et al., 2019b, their Fig. 5e). Therefore, we compare our fixed-N_c results to averages of the last 20 h of their simulations. The systematic difference between the values of cloud-field properties is expected due to differences in the large-scale CCFs; notably, their geostrophic wind speed value is 60 % smaller than that of our simulations (Yamaguchi et al., 2019b, their Table 1). Similarly, we present the results from Seifert et al. (2015), who featured a domain size similar to that of Yamaguchi et al. (2019b) but fixed N_c as in our simulations. We selected their simulations with interactive radiation and prescribed large-scale advective cooling to match our setup as closely as possible. It is worth noting that the cloud fields in Seifert et al. (2015) have larger cloud water and rainwater paths (Fig. 4e and f), which we mainly attribute to their larger meridional geostrophic wind value.

Consistent with Yamaguchi et al. (2019b) and Seifert et al. (2015), increased N_c leads to an increased domain-mean liquid water path, $\mathcal{L}$ (Fig. 4e). As shown by the error bars, the temporal variance in $\mathcal{L}$ increases in response to increased N_c in our simulations. In addition, Fig. 4f illustrates that the domain-mean rainwater path, $\mathcal{R}$, decreases with increasing N_c in all studies. Similar to $\mathcal{L}$, the temporal variations in $\mathcal{R}$ increase with increasing N_c in our simulations. This is in contrast to the small-domain LESs of Yamaguchi et al. (2019b, 50 km × 50 km) and Dagan et al. (2018, 12 km × 12 km–50 km × 50 km), where increased N_c was found to reduce the amplitude of fluctuations in the time series of $\mathcal{R}$. The temporal variance in the liquid water and rainwater path in simulations of Seifert et al. (2015) does not show a systematic response to N_c. Thus, the response of the temporal variations

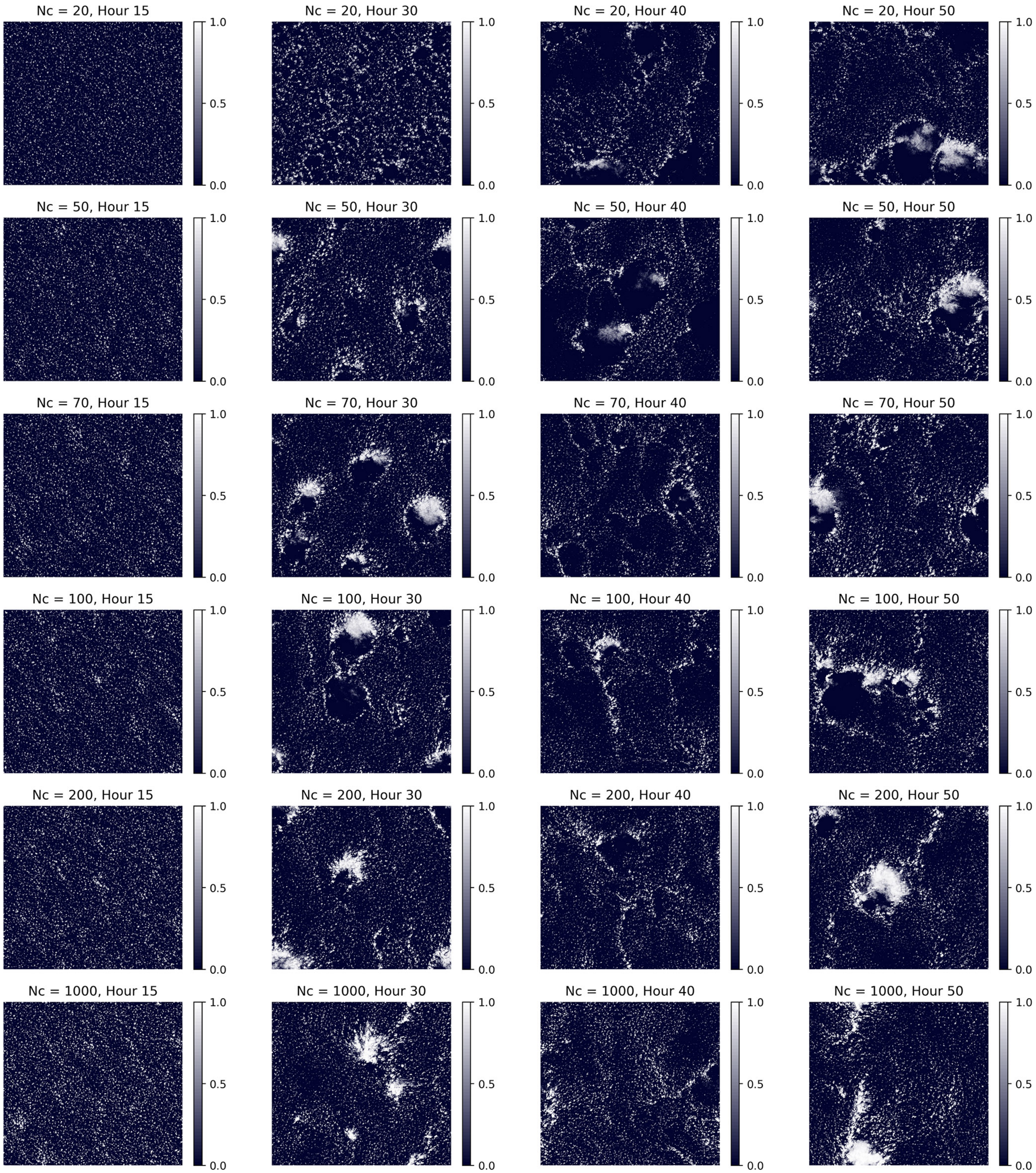

Figure 3. Cloud-field albedo examples. The panels show how cloud fields develop in our LESs featuring the diurnal cycle of insolation with N_c of 20 (first row), 50 (second row), 70 (third row), 100 (fourth row), 200 (fifth row), and 1000 cm^{-3} (sixth row), at hours 15 (first column), 30 (second column), 40 (third column), and 50 (fourth column) after the start of simulations.

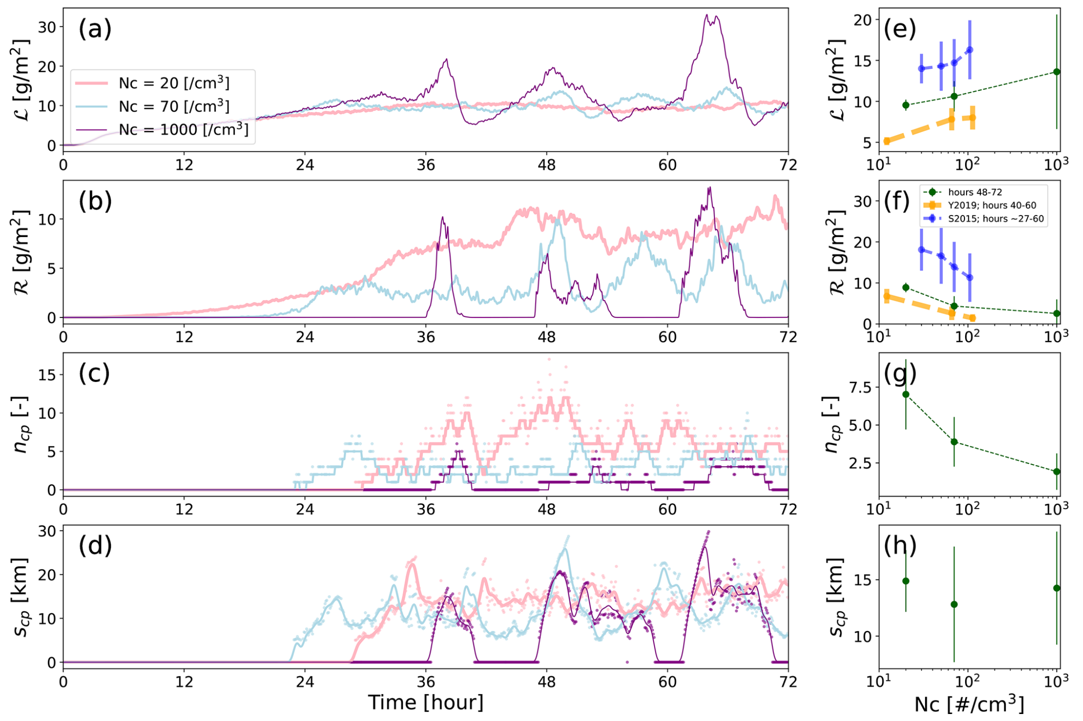

Figure 4. Time series of clouds, rain, and spatial properties of cold pools in simulations without a diurnal cycle. Panels **(a)**–**(d)** show time series of $\mathcal{L}$, $\mathcal{R}$, n_{cp}, and s_{cp} for simulations without the diurnal cycle of solar incoming radiation, where solid lines shown for cold-pool number and size provide a guide to the eye obtained through Gaussian filtering of the original data points. Note that there is significant precipitation in the $N_\text{c} = 20\,\text{cm}^{-3}$ case before cold pools with diameters larger than the 5 km threshold appear. Panels **(e)**–**(h)** show the response of $\mathcal{L}$, $\mathcal{R}$, n_{cp}, and s_{cp} to N_c. The results from Yamaguchi et al. (2019b) averaged over the last 20 h of their simulations are shown in orange. The results from Seifert et al. (2015) for their near-equilibrium state are shown in blue. Dashed lines are added as a visual guide where the mean values show a trend.

in cloud-field properties to N_c appears markedly different in our large domains.

The temporal variations in cold-pool characteristics follow those of the rainwater path, $\mathcal{R}$ (Fig. 4b–d). Notably, in the simulation with $N_\text{c} = 20\,\text{cm}^{-3}$, once cold pools form around hour 30, they grow until around hour 36 and persist until the end of the simulation. In contrast, cold pools in the simulation with $N_\text{c} = 1000\,\text{cm}^{-3}$ form, develop, reach a maximum, decay, and completely vanish. Therefore, increased N_c enhances the intermittency in the evolution of cold pools. Averaged over the last day, increased N_c leads to a smaller number of cold pools, n_{cp} (Fig. 4g), while the domain-mean size of cold pools, s_{cp}, shows a muted response to N_c variations (Fig. 4h).

3.2 Cold-pool evolution shows two distinct mesoscale behaviors for low and high cloud droplet number concentrations

To understand the difference in cold-pool dynamics for different cloud droplet number concentrations, Fig. 5 contrasts the extreme N_c cases. Consistent with observations (Zuidema et al., 2012; Vogel et al., 2021), both have in common that cold pools alter the spatial pattern of moisture in the sub-cloud layer. Cold pools are characterized by relatively dry air inside but relatively moist air at their fronts. Cold pools further modify the spatial pattern of horizontal velocity in the sub-cloud layer, thereby altering the spatial pattern of convergence and, in turn, vertical velocity. Cold pools feature large values of downward vertical velocity inside but strong updrafts at their fronts. Therefore, cold-pool fronts actively contribute to moist convergence and cloud formation. In contrast, the downward motions inside cold pools can potentially suppress convection and lead to cloud-free regions.

Despite the similar evolution of individual cold pools independent of N_c, there are notable differences in the collective, i.e., self-organization, behavior. In the low-N_c simulation (i.e., $N_\text{c} = 20\,\text{cm}^{-3}$), cold pools tend to form in close proximity. As their fronts converge, they trigger the formation of new cold pools at their collision points. This triggering mechanism occurs due to (i) the collision of anomalously moist cold-pool fronts, which mechanically forces the moist air upward due to mass conservation, and (ii) the high efficiency of rain formation, where a small amount of cloud water quickly turns into rainwater, leading to the formation of a new cold pool at the collision point. Consequently, the small,

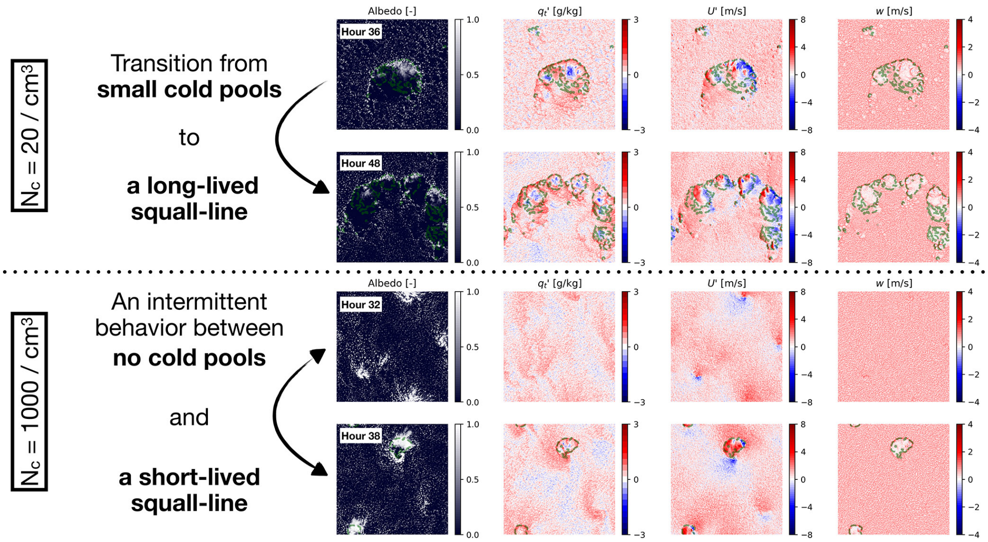

Figure 5. Effects of cold pools on the organization of the (sub-)cloud layer properties for the simulations without a diurnal cycle and with $N_\mathrm{c} = 20$ and $N_\mathrm{c} = 1000\,\mathrm{cm}^{-3}$. For each condition, columns 1–4 indicate the 2D top views of cloud albedo, total moisture anomalies (q_t') at the 200 m level, the horizontal wind speed anomalies (U') at the first level of the model, and the vertical velocity (w) at 200 m height. The dashed green contour line marks the cold-pool boundaries quantified from the mixed-layer height fields. In the U' fields, red indicates that cold pools accelerate the wind, whereas blue indicates that they decelerate it.

space-filling cold pools at hours 30–36 collide and transition into a stage where they become organized into a large front, sustained by the interaction (collision) of its cold pools at its fronts (see Fig. 5, $N_\mathrm{c} = 20\,\mathrm{cm}^{-3}$, hour 48). This is consistent with the time series of cold-pool number (n_cp) and size (s_cp) shown in Fig. 4c and d, which show that the metrics of cold pools stabilize after around hour 38: s_cp remains around 15 ± 5 km, while n_cp remains around 6 ± 4. This behavior of cold pools resembles the mathematical toy model of colliding, circular cold pools presented by Nissen and Haerter (2021, their Fig. 5), which demonstrates (i) similar transitions from randomly distributed cold pools to a band-like structure and (ii) that cold-pool collision is the key mechanism for the self-organization of the system. Notably, their model was motivated by cold pools in the regime of deep convection.

In contrast, cold pools do not interact as readily in the high-N_c simulation (i.e., $N_\mathrm{c} = 1000\,\mathrm{cm}^{-3}$). This is can be attributed to two factors. First, the efficiency of rain formation and, consequently, cold-pool formation, is significantly lower in high-N_c than in low-N_c simulations. Second, cold pools form at greater distances from each other. We speculate that this distance is determined by the horizontal length scale of the self-reinforcing shallow circulations that lead to moisture aggregating in the absence of rain (Bretherton and Blossey, 2017; Narenpitak et al., 2021; Janssens et al., 2023; George et al., 2023). As Janssens et al. (2023) showed, the aggregation of non-precipitating cumuli occurs atop such anomalous mesoscale moist regions, whose size expands in tandem with the growth of anomalous mesoscale dry regions. The scale growth of dry regions in the descending branch of circulations effectively separates moist regions – and consequently, their associated aggregated clouds – preventing interactions between their subsequent cold pools, which form at greater distances from each other. Consistently, Fig. 5 ($N_\mathrm{c} = 1000\,\mathrm{cm}^{-3}$, hour 38) suggests that the downward branches of these circulations are so large that they effectively separate two cloud clusters and cause their cold pools to form at a distance from each other, thus preventing their interactions.

The intermediate case of $N_\mathrm{c} = 70\,\mathrm{cm}^{-3}$ exhibits a cold-pool evolution similar to that of the high-N_c case with $N_\mathrm{c} = 1000\,\mathrm{cm}^{-3}$: (i) cold pools in the $N_\mathrm{c} = 70\,\mathrm{cm}^{-3}$ case also form far apart, resulting in very infrequent cold-pool interactions, and (ii) its cold-pool evolution displays strong intermittency, as shown by Fig. 4c and d. The self-organization dynamics of this case were recently discussed by Alinaghi et al. (2025), in which cold pools are characterized in analogy to squall lines in deep mesoscale convective systems (Rotunno et al., 1988; Weisman and Rotunno, 2004; Stensrud et al., 2005). In this regime, cold pools reinforce and sustain their parent clouds due to the convergence of moist air at their fronts. Once cold pools mature, their moist updrafts at their fronts become so strong that they impinge on the inversion, leading to the formation of stratiform anvils with stratiform precipitation. This weakens the cold-pool-induced updraft, ultimately causing parent clouds to detach from their cold-pool children (Alinaghi et al., 2025, their Figs. 7, 8, and 11). This self-organizing behavior of cold pools and clouds in simulations where they cannot interact is also evident in the cold-pool time series (Fig. 4c and d), which exhibit an intermittent behavior with large amplitudes and low frequencies for both $N_c = 70$ and $1000\,\mathrm{cm}^{-3}$.

An interesting observation is that rain and cold pools tend to develop more rapidly once the initial event has occurred. For instance, the time series shown in Fig. 4b–d demonstrate that it takes approximately 36 h for the $N_c = 1000\,\mathrm{cm}^{-3}$ simulation to produce rain and cold pools. However, subsequent cold-pool events occur within about 8 h, indicating a faster formation of rain and cold pools. In this simulation, the next convective event takes place precisely where the fronts of the previous cold-pool event had accumulated moisture, thereby expediting the development of subsequent convection. We hypothesize that cold pools in the high-N_c simulation act as a "moisture memory" similar to deep convection (Colin et al., 2019), facilitating aggregation over shorter timescales compared to when cold pools are absent. This suggests that the moisture variance induced by cold pools decreases the induced delay in rain formation associated with increased N_c.

As the final point in this section, we investigate how the two N_c-induced regimes of cold-pool self-organization dynamics relate to the mesoscale organization of trade-cumulus cloud fields (Fig. 1, link 2). To address this, we quantify several metrics based on the geometry of clouds that effectively capture the variability in the mesoscale organization of cloud fields in the trades (Janssens et al., 2021). These include the domain-averaged size of cloud objects, the mean fraction of open-sky areas, the domain-mean depth of clouds, and the degree of organization (I_{org}). The details of these metrics and their calculations are explained by Janssens et al. (2021). In addition to geometry-based cloud metrics, we further compute more organization metrics that are based on the spatial distribution of cloud liquid water and total moisture fields. First, we quantify the spatial standard deviation of the liquid water path $\sigma\mathcal{L}$. Second, following Radtke et al. (2023), we consider the metric ΔQ, which quantifies the moisture aggregation at the mesoscales. This metric is calculated as the difference between the 5th and 95th percentiles of the mesoscale total moisture anomaly fields, derived by coarse-graining the total moisture anomaly fields as outlined by Janssens et al. (2023, see their Fig. 3).

Interestingly, the geometry-based organization metrics quantifying the mean size of cloud objects and the open-sky areas, which were shown to explain most of the variability within the mesoscale organization of trade cumuli (Janssens et al., 2021), do not capture the two distinct behaviors of cold pools in low-and high-N_c regimes discussed in the context of Fig. 5 (Fig. A1). However, Fig. 6a and b show that the spatial variance in the cloud liquid water path $\sigma\mathcal{L}$ is strongly affected by N_c. First, increased N_c translates into a strong intermittent behavior in $\sigma\mathcal{L}$ evolution (Fig. 6a). Second, Fig. 6b indicates that, when averaged over 24–48 and 48–72 h intervals, increased N_c leads to greater spatial heterogeneity in the liquid water content: shallow cumuli become more aggregated in response to increased N_c, as visually evident in the snapshots of cloud fields shown in Figs. 3 and 5. The $\sigma\mathcal{L}$–N_c relationship suggests that a reduced number of cold pools, in response to increased N_c, enhances cloud aggregation. This echoes the findings of Radtke et al. (2023), who also showed that rain (auto-conversion) is less efficient in more aggregated fields of trade cumuli (Radtke et al., 2023, their Fig. 2).

With the delay in precipitation formation due to increased N_c, moisture is expected to continue aggregating through shallow circulations driven by latent heating from condensation in the non-precipitating cumulus layer (Bretherton and Blossey, 2017; Janssens et al., 2023). Figure 6c shows that this is exactly what happens in simulations with high N_c. In simulations with N_c of 70 and $1000\,\mathrm{cm}^{-3}$, the moisture aggregation metric ΔQ keeps growing until cold pools start to form, after which ΔQ stabilizes and shows an intermittent behavior. In contrast, in the lowest case of N_c, the moisture does not aggregate at the mesoscales until hour 30, where cold pools start to form, after which the moisture aggregation metric ΔQ starts developing and keeps increasing until the end of the simulation. This implies that this metric of moisture aggregation at the mesoscales is intriguingly able to encapsulate the contrasts between these distinct behaviors of cold pools at low- and high-N_c levels. Averaged over hours 24–48, ΔQ associated with the low-N_c cases is 50 % smaller than of that of the high-N_c cases (Fig. 6d). However, as the simulations progress into hours 48–72, cold pools in low-N_c simulations develop into large squall lines, increasing their moisture aggregation and reducing the sensitivity of ΔQ to N_c (Fig. 6d).

In summary, the evolution of cold pools and trade-cumulus fields is significantly influenced by N_c, exhibiting two distinct behaviors at low and high N_c (Fig. 1, links 1 and 2). In simulations with $N_c = 20\,\mathrm{cm}^{-3}$, cold pools form in close proximity, leading to interactions and collisions that trigger the formation of clouds and, due to high rain efficiency, new cold pools at the collision points. This results in persistent long-lived structures resembling squall lines. Conversely, in simulations with higher N_c values (70 and $1000\,\mathrm{cm}^{-3}$), cold pools form at greater distances, preventing interactions and resulting in intermittent behavior. Cold pools in such cases are short-lived structures resembling squall lines, hypothetically facilitating convection by providing moisture anomalies at their fronts, thereby decreasing N_c-induced delays in subsequent cold-pool formation. This N_c-driven contrast in cold-pool dynamics affects moisture and cloud water variance, with higher N_c leading to more aggregated trade-cumulus cloud fields.

3.3 Diurnal cycle synchronizes the phases of cold-pool evolution across simulations with perturbed N_c

We have shown that the temporal evolution of cold pools (and the trade-cumulus system in general) is controlled by N_c (Fig. 1, links 1 and 2). Observations have shown that the evo-

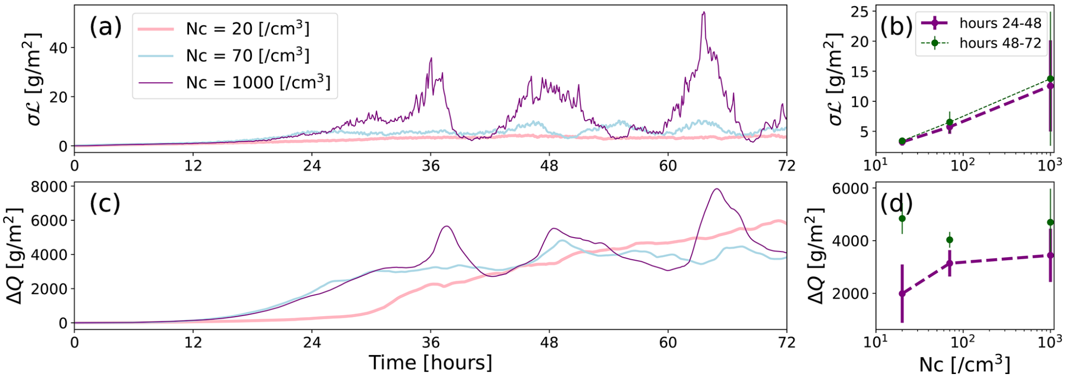

Figure 6. Dependence of mesoscale organization of cloud fields on N_c. Panels **(a)** and **(c)** show the time series of the spatial standard deviation of the liquid water path σL and the difference between the 5th and 95th percentiles of the mesoscale total moisture anomaly fields ΔQ for the simulations without the diurnal cycle of insolation. Panels **(b)** and **(d)** show their responses to N_c for hours 24–48 in purple and hours 48–72 in green. Dashed lines are added as a visual guide where the mean values have a trend.

lution of trade-cumulus fields, their mesoscale organization, precipitation, and cold pools in the trades feature diurnality (Nuijens et al., 2009; Vogel et al., 2021; Vial et al., 2021; Radtke et al., 2022). This raises the following question: "To what extent does the diurnal cycle of insolation, as a time-varying external forcing, control or affect the influence of N_c on the evolution of cold pools (Fig. 1, link 3)?".

To answer this question, we plot the time series of the domain-mean rainwater path ($\mathcal{R}$), the cold-pool number (n_{cp}), and the cold-pool size (s_{cp}) in our simulations with the diurnal cycle, featuring N_c values of 20, 50, 70, 100, 200, and 1000 cm^{-3}. As expected, Fig. 7a–c show that, across all simulations, the evolution of rain and cold pools follows the diurnal cycle of radiation, peaking around sunrise and reaching a minimum around sunset. This pattern is due to the absence of solar radiation combined with longwave radiative cooling during the night. This strong nighttime radiative cooling destabilizes the atmosphere, stimulating convection and leading to the formation of deeper clouds that precipitate more intensely. In contrast, during the daytime, radiative heating from solar radiation stabilizes the atmosphere, suppressing convection and causing a notable decrease in rain and in the number and size of cold pools in almost all simulations. Thus, the diurnal cycle serves as an external forcing (Fig. 1, link 3) that synchronizes the periodicity and amplitude of cold-pool variability that were discussed in the context of Fig. 4 across simulations with different N_c. The simulated diurnal cycle in precipitation and cold pools is consistent with observations of the trades (Nuijens et al., 2009; Vogel et al., 2021; Vial et al., 2021; Radtke et al., 2022).

Although all simulations show evolution synchronized with the diurnal cycle, the cold pools in the simulation with the lowest N_c continue to persist even during the daytime, when convection suppression due to reduced net radiative cooling is at its peak. This behavior is notable as it indicates that the mesoscale self-organization of cold pools through collisions, as discussed in Sect. 3.2, outweighs the externally imposed suppressive effect of the diurnal cycle during the day. Consequently, cold pools in the $N_c = 20\,cm^{-3}$ simulation remain active throughout the day. However, the duration of cold pools' persistence during the day decreases with increasing N_c. Specifically, during daytime hours around 34–46, increased N_c leads to an earlier disappearance of cold pools and a more delayed formation of the next generation of cold pools, as shown in Fig. 7c. To summarize, we find that the diurnal cycle externally synchronizes the mesoscale self-organization dynamics of cold pools, which is in turn modulated by the details of microphysics and rain formation.

The synchronization of cold-pool events by the diurnal cycle enables us to compare the responses of the rainwater path ($\mathcal{R}$) and cold pools to N_c during the same time window across all simulations. In all simulations, except for $N_c = 20\,cm^{-3}$, rain and, subsequently, cold pools begin to form after hour 24 (Fig. 7a–c), with the evolution of cold pools following the diurnal cycle of net radiative cooling. We refer to the day starting at hour 22 as the "transient" phase and the subsequent day beginning at hour 46 as the "near-equilibrium" phase. We selected these hours based on the development of the total water (cloud and water vapor) path in our simulations, which consistently increases until hour 48 across all simulations, after which it stabilizes and becomes time-invariant (Fig. A2).

All simulations consistently show a higher daily mean rainwater path ($\mathcal{R}$) during the near-equilibrium phase compared to the transient phase (Fig. 7d). This is because, in the near-equilibrium phase, our simulations are more developed and feature deeper boundary layers with larger total water that can develop more rain. Consistent with our results based on the last 24 h of simulations without the diurnal cycle (Fig. 4f–h), Fig. 7d and e illustrate that, during the both transient and near-equilibrium phases, the rainwater path ($\mathcal{R}$) and the cold-pool number (n_{cp}) decrease with increasing N_c.

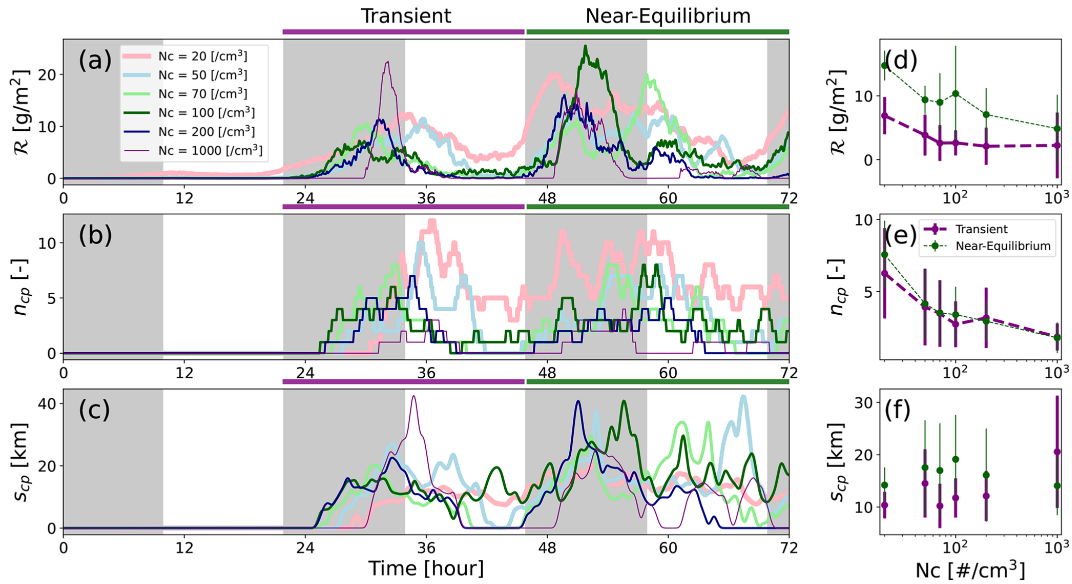

Figure 7. Effects of the diurnal cycle of insolation on the evolution and N_c response of rain and cold pools. Panels **(a)–(c)** show time series of the rainwater path ($\mathcal{R}$), cold-pool number (n_{cp}), and cold-pool size (s_{cp}) for simulations with the diurnal cycle of solar incoming radiation. Nighttime is shown by the gray color. Solid lines shown for cold-pool number and size provide a guide to the eye obtained through Gaussian filtering of the original data points. Note that there is significant precipitation in the $N_c = 20\,\mathrm{cm}^{-3}$ case before cold pools with diameters larger than the 5 km threshold appear. Panels **(d)**, **(e)**, and **(f)** show the response of $\mathcal{R}$, n_{cp}, and s_{cp} to N_c during the transient (purple) and near-equilibrium (green) phases, which are marked in the time series plots **(a)**, **(b)**, and **(c)**, respectively. Dashed lines are added as a visual guide where there is a trend.

Also, the cold-pool size (s_{cp}) does not show a notable change in response to N_c (Fig. 7f).

3.4 The Twomey effect primarily controls the dependence of the cloud radiative effect on N_c

In this section, we investigate the sensitivity of the relative cloud radiative effect (Xie and Liu, 2013), rCRE $= f_c \cdot \mathcal{A}_c$, to N_c (Fig. 1, link 4), where f_c and $\mathcal{A}_c$ are the respective cloud fraction and albedo. Assuming the plane-parallel approximation (Lacis and Hansen, 1974), cloud albedo is given by $\mathcal{A}_c = \frac{\tau}{\tau+7.7}$, with a cloud optical thickness $\tau \approx {N_c}^{1/3}\mathcal{L}^{5/6}$ following Zhang et al. (2005). Therefore, we explore the response of the cloud fraction (f_c), domain-mean liquid water path ($\mathcal{L}$), mean cloud albedo ($\mathcal{A}_c$) over the cloudy columns where the cloud liquid water path is larger than zero, and the relative cloud radiative effect (rCRE) to N_c. These sensitivities are explored during different phases of the simulations with the diurnal cycle: non-precipitating (hours 5–15), transient (hours 22–46), and near-equilibrium (hours 46–72) phases. For comparison, we also include results from Seifert et al. (2015) and Yamaguchi et al. (2019b), where the latter features more comprehensive microphysics than our study with its fixed cloud droplet number concentration.

During the non-precipitating (or weakly precipitating) phase, the response of the cloud fraction (f_c) and liquid water path ($\mathcal{L}$) to N_c is negligible (Fig. 8a and b). Thus, the relative cloud radiative effect (rCRE) is influenced by N_c primarily through the cloud albedo response, or the Twomey effect (Fig. 8c and d). During both the transient and near-equilibrium phases, the cloud fraction (f_c) decreases very slightly with increasing N_c, although this response is much smaller than the temporal variance in f_c within each simulation (Fig. 8a). Additionally, the liquid water path ($\mathcal{L}$) shows a small increase with increased N_c (Fig. 8b). However, similar to the non-precipitating phase, the Twomey effect continues to strongly control the response of rCRE to N_c during both the transient and near-equilibrium phases (Fig. 8c and d).

The response of the liquid water path in the near-equilibrium phase is consistent with the results of Yamaguchi et al. (2019b) and Seifert et al. (2015). This small positive sensitivity of the liquid water path in our simulations does not significantly affect the impact of N_c on rCRE compared to the Twomey effect. The cloud fraction (f_c) decreases with increasing N_c in the simulations of Yamaguchi et al. (2019b). Similarly, our simulations and those of Seifert et al. (2015) both show a decrease in f_c in response to increased N_c. However, this decrease seems to be smaller compared with the f_c response in the simulations of Yamaguchi et al. (2019b). It would be interesting to revisit this difference with a cloud microphysics scheme that does not fix the cloud droplet number, as in the current study, but rather allows for full microphysical adjustments.

It is worth noting that, although variations in N_c modulate the number of cold pools and, in turn, mesoscale

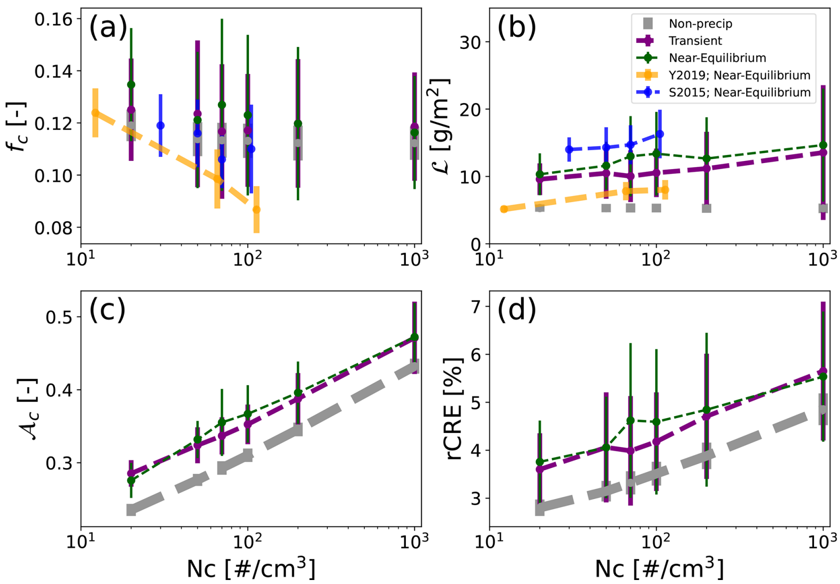

Figure 8. Sensitivity of the relative cloud radiative effect to cloud droplet number. Panels **(a)–(d)** show the response of the cloud fraction (f_c), domain-mean liquid water path ($\mathcal{L}$), cloud albedo ($\mathcal{A}_c$), and relative cloud radiative effect (rCRE) to N_c during the non-precipitating (dark gray), transient (purple), and near-equilibrium (green) phases. The results from Yamaguchi et al. (2019b) averaged over the last 20 h of their simulations are shown in orange. The results from Seifert et al. (2015) for their near-equilibrium state are shown in blue. Note that Yamaguchi et al. (2019b) and Seifert et al. (2015) do not report on the cloud albedo and rCRE in their studies. Dashed lines are added as a visual guide where there is a trend.

self-organization of trade-cumulus fields, the cloud fraction (f_c) is very weakly affected. Our results here resonate with Janssens et al. (2025), who hypothesized that circulations associated with self-organization symmetrically distribute cloudiness at the mesoscales such that the increased cloudiness at their ascending branch is compensated for by the decreased cloudiness at their descending branch. This implies that, although decreased N_c increases the number of cold pools, the increased cloudiness at their fronts, where convection is triggered, appears to be buffered by the decreased cloudiness at their interiors, where convection is suppressed. Future studies are encouraged to explicitly investigate this.

3.5 N_c induces comparable variations in cloud radiative effect to the large-scale cloud-controlling factors

In this section, we quantify the relative importance of N_c (Fig. 1, link 1) compared with the large-scale cloud-controlling factors (CCFs; Fig. 1, link 3) with respect to driving changes in cloud-field properties and radiative effects (Fig. 1, links 2 and 4). Using the data from the Cloud Botany dataset (Jansson et al., 2023a) as well as our new simulations of this study, we employ a multivariate regression model:

$$\overline{C} \approx \sum_{i=1}^{7} \beta_i \times \widetilde{\mathrm{CCF}}_i \quad \text{with} \quad \widetilde{\mathrm{CCF}}_i := \frac{\mathrm{CCF}_i - \overline{\mathrm{CCF}}_i}{\sigma(\mathrm{CCF}_i)},$$

where the vector $\overline{C}$ represents the mean of the metric $C \in \{\mathcal{A}_c, \mathrm{rCRE}\}$, averaged over the last 2 d (hours 12–60) for each member of the Cloud Botany ensemble. Each regressor $\widetilde{\mathrm{CCF}}_i$ is a vector containing the associated CCF_i values for the simulation members of the Cloud Botany ensemble. The regressors (CCFs) include sea-surface (potential) temperature (θ_{l0}), near-surface wind speed (u_0), moisture scale height (h_{q_t}), temperature lapse rate (Γ), large-scale vertical velocity variability (w_1), and horizontal wind shear (u_z). In addition, we consider N_c as a seventh regressor. For the regressor N_c, we use the simulations with the diurnal cycle over hours 12–60 to be consistent with the simulations of the Cloud Botany ensemble. All regressors are standardized by subtracting their mean $\overline{\mathrm{CCF}}$ and dividing by their standard deviation $\sigma(\mathrm{CCF})$ across the ensemble, which allows the comparison of CCFs and N_c with an equal weighting. In our regression analysis, we only include simulations that develop clouds and run for at least 48 h. This leaves us with 80 simulations out of the initial 103 in the Cloud Botany ensemble. Including the simulations with the diurnal cycle from this study (six in total) and noting that the simulation with $N_c = 70\,\mathrm{cm}^{-3}$ is already part of the ensemble as the central reference simulation, our regression analysis features 85 data points in total. This means that the target value $\overline{C}$ and regressors $\widetilde{\mathrm{CCF}}_i$ of the regression model are vectors of size 85×1.

Figure 9 shows the results of the multivariate regression for cloud albedo ($\mathcal{A}_c$) and relative cloud radiative effect (rCRE). Note that the response of $\mathcal{A}_c$ and rCRE to the CCFs of the Cloud Botany ensemble has already been addressed and discussed by Janssens (2023a) and Janssens et al. (2025),

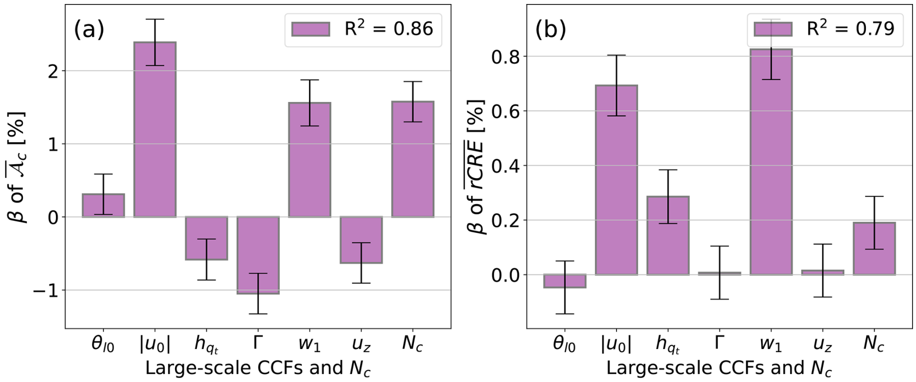

Figure 9. Cloud-field response to large-scale cloud-controlling factors and cloud droplet number concentration. The standardized β coefficients of the multiple regression analysis for **(a)** cloud albedo ($\mathcal{A}_c$) and **(b)** relative cloud radiative effect (rCRE), all averaged over the last 2 d of the LESs of the Cloud Botany ensemble. The error bars show the 95 % confidence interval for each regressor. The p values of the F test of all models are smaller than 10^{-22}.

and we refer the reader to these publications for further details. Figure 9a illustrates that the effect of N_c on $\mathcal{A}_c$, known as the Twomey effect, is comparable to that of large-scale subsidence as quantified by w_1. Additionally, the effect of N_c on trade-cumulus brightening is about 75 % of the effect of horizontal wind speed, 150 % of the effect of stability, and 300 % of the effects of free-tropospheric humidity and vertical wind shear. Eventually, the response of rCRE to N_c is statistically significant at the 95 % level and accounts for about 66 %, 28 %, and 25 % of the response of rCRE to free-tropospheric humidity, wind speed, and large-scale subsidence, respectively (Fig. 9b). Note that the sensitivity of rCRE to N_c is smaller than that of cloud albedo to N_c in our regression analysis, which is due to the very weak impact of N_c on f_c (Fig. 8a). Similar regression results for other cloud-field and cold-pool properties are presented in Fig. A3.

4 Conclusions and outlook

Cold pools, resulting from rain evaporation, affect the mesoscale organization of trade-cumulus fields (Zuidema et al., 2012; Seifert and Heus, 2013; Vogel et al., 2016, 2021; Alinaghi et al., 2025). We have used an ensemble of large-domain LESs to investigate the sensitivity of mesoscale organization to the cloud droplet number concentration (N_c) and the role of cold pools therein, as conceptualized in Fig. 1.

Investigating the sensitivity of mesoscale cold-pool dynamics to microphysics (Fig. 1, link 1), we find that cold pools show two distinct behaviors at low and high N_c. In low-N_c cases, there are many cold pools within the simulation domain, which form in close proximity (Fig. 4c, d, g and h and Fig. 5). This allows them to interact with each other through collisions. Efficient rain formation then leads to the swift triggering of new cold pools at collision points. Consequently, cold pools organize into a large, long-lived front with a resemblance to a squall line that perpetuates through the collisions of cold pools at its leading edge. In contrast, high-N_c cases feature sparsely distributed cold pools, with this sparse distribution preventing their interaction. In this regime, cold pools exhibit an intermittent behavior, manifesting as small, short-lived fronts resembling squall lines that form, develop, decay, and vanish (Fig. 4c, d, g, and h and Fig. 5).

For the effect of N_c on the interaction between clouds and cold pools (Fig. 1, link 2), our analysis shows that increased N_c suppresses the formation of cold pools (Fig. 4g and h and Fig. 5), while enhancing the self-aggregation of cloud fields (Fig. 6). In other words, by delaying precipitation formation, increased N_c allows non-precipitating cumulus fields to aggregate moisture (Fig. 6c and d) through self-reinforcing mesoscale overturning circulations (Bretherton and Blossey, 2017; Narenpitak et al., 2021; Janssens et al., 2023). We quantified this effect, which clearly influences the mesoscale organization of cloud fields, particularly by increasing the spatial variance in the cloud liquid water path (Fig. 6a and b). Interestingly, despite the suppression of cold pools and the boost in aggregation due to increased N_c (Fig. 6a–d), the overall daily mean responses of the cloud fraction and liquid water path are notably small (Fig. 4e and Fig. 8a and b). This echoes the recent findings of Janssens et al. (2025), who reported that shallow mesoscale circulations appear to symmetrically modulate cloudiness within trade-cumulus fields such that the increased cloudiness at their ascending branch is compensated for by the decreased cloudiness at their descending branch. This suggests that, although mesoscale organization is affected by the variations in cold pools due to increasing N_c, the increased cloudiness at the edges of cold pools appears to be buffered by the decreased cloudiness at their interiors.

For the effect of the diurnal cycle as an external forcing on the microphysical sensitivity (Fig. 1, link 3), we find that the diurnal cycle synchronizes the self-organization dynamics of cold pools on the mesoscale across simulations with varying N_c (Fig. 7). Thus, cold-pool activity is controlled by both the external forcing and the self-organization dynamics. The contribution of self-organization dynamics increases with decreasing N_c as showcased by the fact that cold-pool activity survives the daytime suppression for the lowest N_c case (Fig. 7b and c).

To compare the importance of microphysical and large-scale controls on the cold-pool dynamics (Fig. 1, links 1 and 3) occurring on the intermediate mesoscale, we have made use of the Cloud Botany ensemble (Jansson et al., 2023a). We demonstrate that the Twomey effect is as significant as the primary cloud-controlling factors for the brightening of trade-cumulus fields (Fig. 9a). Despite the very small response of the cloud fraction to N_c (Fig. 8a), the response of the relative cloud radiative effect to N_c (Fig. 1, link 4) is about 25 % as significant as the response of rCRE to horizontal wind speed and large-scale subsidence (Fig. 9b).

We have obtained these results using a prescribed cloud droplet number as a proxy for microphysical influences. This assumption excludes microphysical adjustments. Despite a broad agreement between our results and those of Yamaguchi et al. (2019b) that are based on a more detailed microphysics scheme with prognostic N_c, Li et al. (2015) showed that cold pools are sensitive to choices of microphysics schemes. We, therefore, encourage future research, such as the Cold Pool Model Intercomparison Project (CP-MIP; Kazil et al., 2025), to focus on the sensitivity of mesoscale cold-pool dynamics to such microphysical choices if we truly want to understand rain evaporation, cold pools, and their relevance for trade-cumulus fields.

Irrespective of its idealizations, this study clearly highlights that aerosol–cloud interactions are affected by processes happening at multiple spatial and temporal scales, ranging from the microscale via the mesoscale to the large scales. For shallow cloud fields in the trades, we demonstrate that variations in the microscale can manifest themselves at the mesoscale to a degree that is comparable to the influence of large-scale controls. We consider these findings a valuable step towards understanding the mesoscales as a prerequisite for constraining trade-cumulus–climate feedbacks as well as trade-cumulus-mediated aerosol forcings.

Appendix A: Supplementary figures

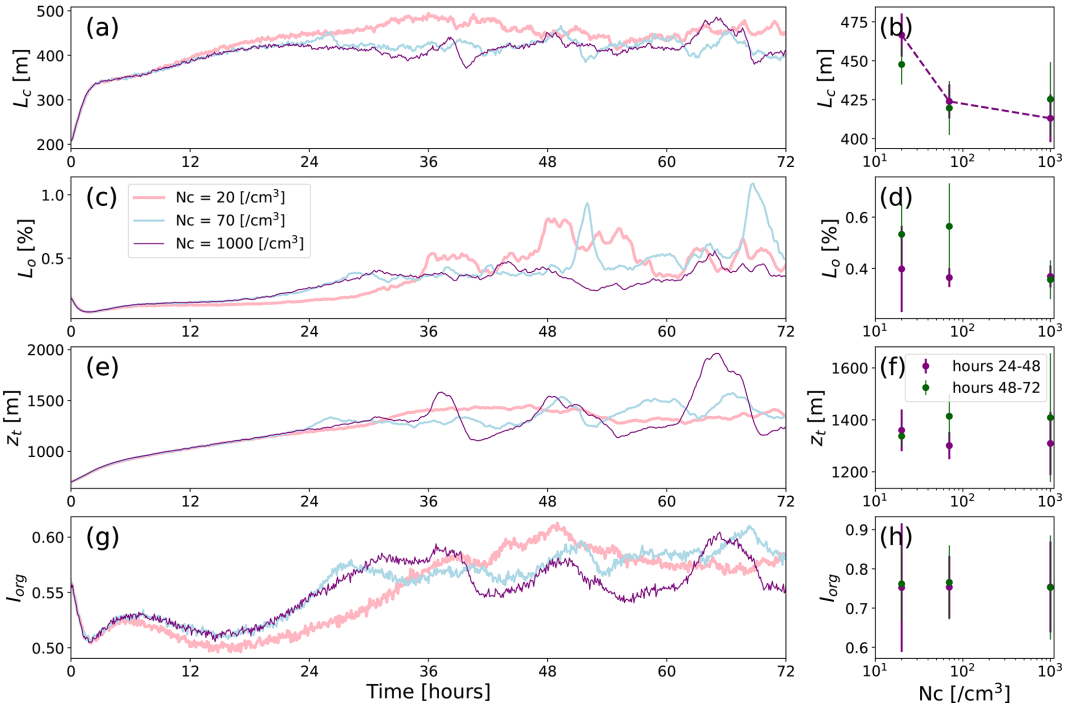

Figure A1. Dependence of several mesoscale cloud organization metrics on N_c. Panels **(a)**, **(c)**, **(e)**, and **(g)** show the time series of the domain-mean size of cloud objects (L_c), the mean fraction of the open-sky areas (L_o), the domain-mean of cloud-top height (z_t), and the degree of organization (I_{org}) for the simulations without the diurnal cycle of insolation. Panels **(b)**, **(d)**, **(f)**, and **(h)** show their mean responses to N_c for hours 24–48 in purple and 48–72 in green. The dashed line is shown as a visual guide where there is a trend.

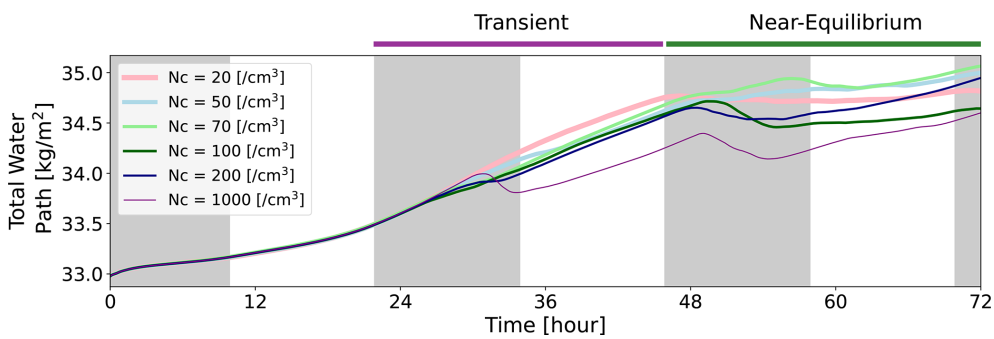

Figure A2. Total water path time series for several values of N_c. The figure shows the development of the domain-mean total water path, which is the sum of both the cloud water and water vapor paths. The transient and near-equilibrium phases are marked by purple and green, respectively.

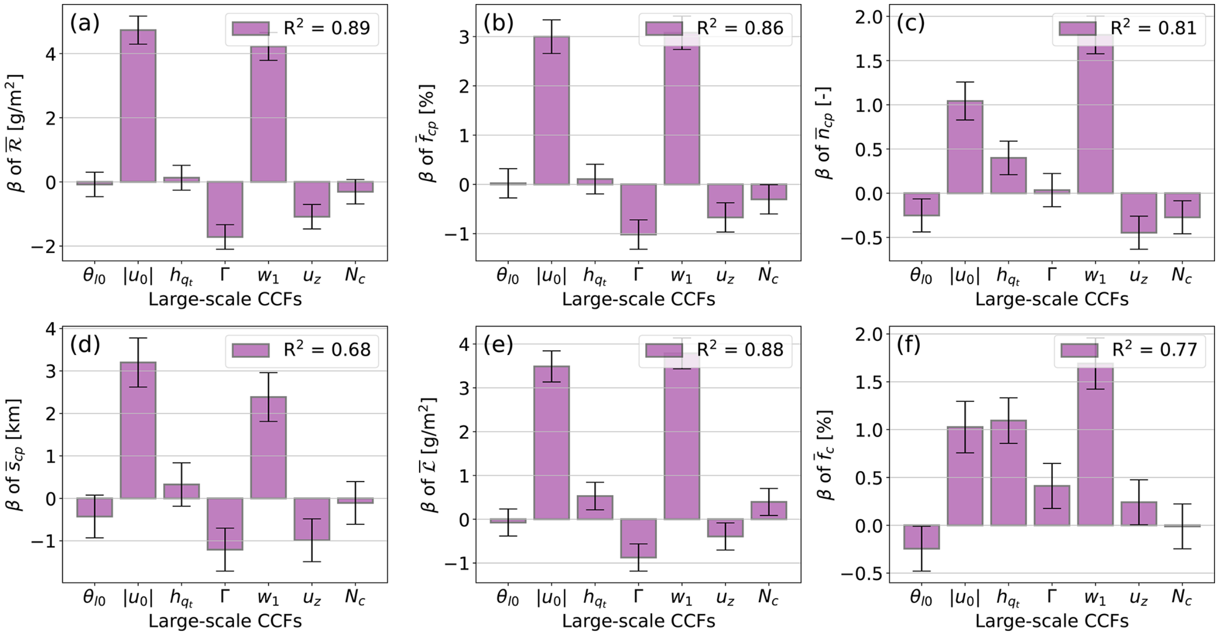

Figure A3. Cloud-field response to large-scale cloud-controlling factors and cloud droplet number perturbations. The standardized β coefficients of the multiple regression analysis for the **(a)** rainwater path ($\overline{\mathcal{R}}$), **(b)** cold-pool fraction ($\overline{f}_{cp}$), **(c)** cold-pool number ($\overline{n}_{cp}$), **(d)** cold-pool size ($\overline{s}_{cp}$) **(e)** liquid water path ($\overline{\mathcal{L}}$), and **(f)** cloud fraction ($\overline{f}_c$), all averaged over the last 2 d of the LESs of the Cloud Botany ensemble. The error bars show the 95 % confidence interval for each regressor. The larger the distance of the confidence interval from zero, the more significant the corresponding regressor. The p values of the F test of all models are smaller than 10^{-15}.

Code and data availability. The Cloud Botany dataset is publicly accessible through the EUREC^{4}A intake catalog (https://howto.eurec4a.eu/botany_dales.html, Jansson et al., 2023b). The simulation outputs of Yamaguchi et al. (2019b) are publicly available from the NOAA dataset platform (https://csl.noaa.gov/groups/csl9/datasets/data/cloud_phys/2019-Yamaguchi-Feingold-Kazil/, Yamaguchi et al., 2019). The data were analyzed using the following Python libraries: NumPy (https://github.com/numpy/numpy, NumPy, 2025), Xarray (https://github.com/pydata/xarray, Xarray, 2025), pandas (https://github.com/pandas-dev/pandas, Pandas, 2025), SciPy (https://github.com/scipy/scipy, SciPy, 2025), statsmodel (https://github.com/statsmodels/statsmodels, Statsmodels, 2025), Matplotlib (https://github.com/matplotlib/matplotlib, Matplotlib, 2025), and seaborn (https://github.com/mwaskom/seaborn, Seaborn, 2025). The basic profiles and time series associated with cloud-field properties, cloud organization metrics, and cold-pool properties as well as a movie of simulations are publicly available in Alinaghi et al. (2024b) and from https://doi.org/10.5281/zenodo.13868738. The coarse-graining of the total water path anomaly fields was done using the code (SMOCs.ipynb) from Janssens (2023b), which is publicly available (https://doi.org/10.5281/zenodo.8089287).

Author contributions. The concept for this study was developed by PA and FG. LESs were performed by FJ. PA analyzed and visualized the data, with DAB assisting during the analysis. PA and FG interpreted the results with contributions from FJ and DAB. PA drafted the initial manuscript, and all authors contributed to its revision and finalization.

Competing interests. At least one of the (co-)authors is a member of the editorial board of *Atmospheric Chemistry and Physics*. The peer-review process was guided by an independent editor, and the authors also have no other competing interests to declare.

Disclaimer. Views and opinions expressed in the paper are those of the author(s) only and do not necessarily reflect those of the European Union or the European Research Council Executive Agency. Neither the European Union nor the granting authority can be held responsible for them.

Acknowledgements. Pouriya Alinaghi and Fredrik Jansson thank SURF (https://www.surf.nl, last access: 15 March 2025) for making the Dutch National Supercomputer Snellius accessible for running and analyzing the droplet number simulations.

Financial support. This research has been supported by the Branco Weiss Fellowship – Society in Science, the European Research Council Horizon Europe program (grant no. 101117462), and the European Union's Horizon 2020 Research and Innovation program (CONSTRAIN project; grant no. 820829).

Review statement. This paper was edited by Raphaela Vogel and reviewed by two anonymous referees.

References

Albrecht, B. A.: Aerosols, Cloud Microphysics, and Fractional Cloudiness, Science, 245, 1227–1230, https://doi.org/10.1126/science.245.4923.1227, 1989.

Alinaghi, P., Janssens, M., Choudhury, G., Goren, T., Siebesma, A. P., and Glassmeier, F.: Shallow cumulus cloud fields are optically thicker when they are more clustered, Q. J. Roy. Meteor. Soc., 150, 3566–3577, https://doi.org/10.1002/qj.4783, 2024a.

Alinaghi, P., Jansson, F., A. Blázquez, D., and Glassmeier, F.: Datasets and the movie for the manuscript "Cold pools mediate mesoscale adjustments of trade-cumulus fields to changes in cloud-droplet number concentration", Zenodo [data set], https://doi.org/10.5281/zenodo.13868738, 2024b.

Alinaghi, P., Siebesma, A. P., Jansson, F., Janssens, M., and Glassmeier, F.: External Drivers and Mesoscale Self-Organization of Shallow Cold Pools in the Trade-Wind Regime, J. Adv. Model. Earth Sy., 17, e2024MS004540, https://doi.org/10.1029/2024MS004540, 2025.

Bellouin, N., Quaas, J., Gryspeerdt, E., Kinne, S., Stier, P., Watson-Parris, D., Boucher, O., Carslaw, K. S., Christensen, M., Daniau, A.-L., Dufresne, J.-L., Feingold, G., Fiedler, S., Forster, P., Gettelman, A., Haywood, J. M., Lohmann, U., Malavelle, F., Mauritsen, T., McCoy, D. T., Myhre, G., Mülmenstädt, J., Neubauer, D., Possner, A., Rugenstein, M., Sato, Y., Schulz, M., Schwartz, S. E., Sourdeval, O., Storelvmo, T., Toll, V., Winker, D., and Stevens, B.: Bounding global aerosol radiative forcing of climate change, Rev. Geophys., 58, e2019RG000660, https://doi.org/10.1029/2019RG000660, 2020.

Böing, S. J., Jonker, H. J., Siebesma, A. P., and Grabowski, W. W.: Influence of the subcloud layer on the development of a deep convective ensemble, J. Atmos. Sci., 69, 2682–2698, 2012.

Bony, S., Stevens, B., Ament, F., Bigorre, S., Chazette, P., Crewell, S., Delanoë, J., Emanuel, K., Farrell, D., Flamant, C., Gross, S., Hirsch, L., Karstensen, J., Mayer, B., Nuijens, L., Ruppert Jr., J. H.,, Sandu, I., Siebesma, A. P., Speich, S., Szczap, F., Totems, J., Vogel, R., Wendisch, M., and Wirth, M.: EUREC 4A: A field campaign to elucidate the couplings between clouds, convection and circulation, Surv. Geophys., 38, 1529–1568, https://doi.org/10.1007/s10712-017-9428-0, 2017.

Bony, S., Schulz, H., Vial, J., and Stevens, B.: Sugar, gravel, fish, and flowers: Dependence of mesoscale patterns of trade-wind clouds on environmental conditions, Geophys. Res. Lett., 47, e2019GL085988, https://doi.org/10.1029/2019GL085988, 2020.

Bony, S., Lothon, M., Delanoë, J., Coutris, P., Etienne, J.-C., Aemisegger, F., Albright, A. L., André, T., Bellec, H., Baron, A., Bourdinot, J.-F., Brilouet, P.-E., Bourdon, A., Canonici, J.-C., Caudoux, C., Chazette, P., Cluzeau, M., Cornet, C., Desbios, J.-P., Duchanoy, D., Flamant, C., Fildier, B., Gourbeyre, C., Guiraud, L., Jiang, T., Lainard, C., Le Gac, C., Lendroit, C., Lernould, J., Perrin, T., Pouvesle, F., Richard, P., Rochetin, N., Salaün, K., Schwarzenboeck, A., Seurat, G., Stevens, B., Totems, J., Touzé-Peiffer, L., Vergez, G., Vial, J., Villiger, L., and Vogel, R.: EUREC^{4}A observations from the SAFIRE ATR42 aircraft, Earth Syst. Sci. Data, 14, 2021–2064, https://doi.org/10.5194/essd-14-2021-2022, 2022.

Bretherton, C. and Blossey, P.: Understanding mesoscale aggregation of shallow cumulus convection using large-eddy simulation, J. Adv. Model. Earth Sy., 9, 2798–2821, 2017.

Cesana, G. V. and Del Genio, A. D.: Observational constraint on cloud feedbacks suggests moderate climate sensitivity, Nat. Clim. Change, 11, 213–218, https://doi.org/10.1038/s41558-020-00970-y, 2021.

Colin, M., Sherwood, S., Geoffroy, O., Bony, S., and Fuchs, D.: Identifying the Sources of Convective Memory in Cloud-Resolving Simulations, J. Atmos. Sci., 76, 947–962, https://doi.org/10.1175/JAS-D-18-0036.1, 2019.

Colón-Robles, M., Rauber, R. M., and Jensen, J. B.: Influence of low-level wind speed on droplet spectra near cloud base in trade wind cumulus, Geophys. Res. Lett., 33, L20814, https://doi.org/10.1029/2006GL027487, 2006.

Dagan, G., Koren, I., Kostinski, A., and Altaratz, O.: Organization and oscillations in simulated shallow convective clouds, J. Adv. Model. Earth Sy., 10, 2287–2299, 2018.

Denby, L.: Charting the Realms of Mesoscale Cloud Organisation using Unsupervised Learning, arXiv [preprint], https://doi.org/10.48550/arXiv.2309.08567, 2023.

Drager, A. J. and van den Heever, S. C.: Characterizing convective cold pools, J. Adv. Model. Earth Sy., 9, 1091–1115, https://doi.org/10.1002/2016MS000788, 2017.

George, G., Stevens, B., Bony, S., Vogel, R., and Naumann, A. K.: Widespread shallow mesoscale circulations observed in the trades, Nat. Geosci., 16, 584–589, 2023.

Gerber, H. E., Frick, G. M., Jensen, J. B., and Hudson, J. G.: Entrainment, Mixing, and Microphysics in Trade-Wind Cumulus, J. Meteorol. Soc. Jpn. Ser. II, 86A, 87–106, https://doi.org/10.2151/jmsj.86A.87, 2008.

Glassmeier, F. and Feingold, G.: Network approach to patterns in stratocumulus clouds, P. Natl. Acad. Sci. USA, 114, 10578–10583, https://doi.org/10.1073/pnas.1706495114, 2017.

Glassmeier, F., Hoffmann, F., Johnson, J. S., Yamaguchi, T., Carslaw, K. S., and Feingold, G.: Aerosol-cloud-climate cooling overestimated by ship-track data, Science, 371, 485–489, https://doi.org/10.1126/science.abd3980, 2021.

Haerter, J. O. and Schlemmer, L.: Intensified cold pool dynamics under stronger surface heating, Geophys. Res. Lett., 45, 6299–6310, https://doi.org/10.1029/2017GL076874, 2018.

Haerter, J. O., Böing, S. J., Henneberg, O., and Nissen, S. B.: Circling in on convective organization, Geophys. Res. Lett., 46, 7024–7034, 2019.

Harris, C. R., Millman, K. J., van der Walt, S. J., Gommers, R., Virtanen, P., Cournapeau, D., Wieser, E., Taylor, J., Berg, S., Smith, N. J., Kern, R., Picus, M., Hoyer, S., van Kerkwijk, M. H., Brett, M., Haldane, A., del Río, J. F., Wiebe, M., Peterson, P., Gérard-Marchant, P., Sheppard, K., Reddy, T., Weckesser, W., Abbasi, H., Gohlke, C., and Oliphant, T. E.: Array programming with NumPy, Nature, 585, 357–362, https://doi.org/10.1038/s41586-020-2649-2, 2020.

Helfer, K. C. and Nuijens, L.: The Morphology of Simulated Trade-Wind Convection and Cold Pools Under Wind Shear, J. Geophys. Res.-Atmos., 126, e2021JD035148, https://doi.org/10.1029/2021JD035148, 2021.

Hersbach, H., Bell, B., Berrisford, P., Hirahara, S., Horányi, A., Muñoz-Sabater, J., Nicolas, J., Peubey, C., Radu, R., Schepers, D., Simmons, A., Soci, C., Abdalla, S., Abellan, X., Balsamo, G., Bechtold, P., Biavati, G., Bidlot, J., Bonavita, M., De Chiara, G., Dahlgren, P., Dee, D., Diamantakis, M., Dragani, R., Flemming, J., Forbes, R., Fuentes, M., Geer, A., Haimberger, L., Healy, S., Hogan, R. J., Hólm, E., Janisková, M., Keeley, S., Laloyaux, P., Lopez, P., Lupu, C., Radnoti, G., de Rosnay, P., Rozum, I., Vamborg, F., Villaume, S., and Thépaut, J.-N.: The ERA5 global reanalysis, Q. J. Roy. Meteor. Soc., 146, 1999–2049, https://doi.org/10.1002/qj.3803, 2020.

Hoyer, S. and Joseph, H.: xarray: N-D labeled Arrays and Datasets in Python, Journal of Open Research Software, 5, 10, https://doi.org/10.5334/jors.148, 2017.

Hudson, J. G. and Noble, S.: Low-altitude summer/winter microphysics, dynamics, and CCN spectra of northeastern Caribbean small cumuli, and comparisons with stratus, J. Geophys. Res.-Atmos., 119, 5445–5463, https://doi.org/10.1002/2013JD021442, 2014.

Hunter, J. D.: Matplotlib: A 2D graphics environment, Comput. Sci. Eng., 9, 90–95, https://doi.org/10.1109/MCSE.2007.55, 2007.

IPCC AR6: The Earth's Energy Budget, Climate Feedbacks and Climate Sensitivit, Chap. 7, Cambridge University Press, 923–1054, https://doi.org/10.1017/9781009157896.009, 2023.

Janssens, M.: Mesoscale Cloud Patterns in the Trade-Wind Boundary Layer, PhD thesis, Wageningen University, https://doi.org/10.18174/635857, 2023a.

Janssens, M.: Supporting data for Chap. 7 of "Mesoscale Cloud Patterns in the Trade-Wind Boundary Layer", Zenodo [code], https://doi.org/10.5281/zenodo.8089287, 2023b.

Janssens, M., Vilà-Guerau de Arellano, J., Scheffer, M., Antonissen, C., Siebesma, A. P., and Glassmeier, F.: Cloud patterns in the trades have four interpretable dimensions, Geophys. Res. Lett., 48, e2020GL091001, https://doi.org/10.1029/2020GL091001, 2021.

Janssens, M., De Arellano, J. V.-G., Van Heerwaarden, C. C., De Roode, S. R., Siebesma, A. P., and Glassmeier, F.: Nonprecipitating Shallow Cumulus Convection Is Intrinsically Unstable to Length Scale Growth, J. Atmos. Sci., 80, 849–870, 2023.

Janssens, M., Jansson, F., Alinaghi, P., Glassmeier, F., and Siebesma, A. P.: Symmetry in Mesoscale Circulations Explains Weak Impact of Trade Cumulus Self-Organization on the Radiation Budget in Large-Eddy Simulations, Geophys. Res. Lett., 52, e2024GL112288, https://doi.org/10.1029/2024GL112288, 2025.

Jansson, F., Janssens, M., Grönqvist, J. H., Siebesma, A. P., Glassmeier, F., Attema, J., Azizi, V., Satoh, M., Sato, Y., Schulz, H., and Kölling, T.: Cloud Botany: Shallow Cumulus Clouds in an Ensemble of Idealized Large-Domain Large-Eddy Simulations of the Trades, J. Adv. Model. Earth Sy., 15, e2023MS003796, https://doi.org/10.1029/2023MS003796, 2023a.

Jansson, F., Janssens, M., and Schulz, H.: Cloud Botany with DALES. How to EUREC^{4}A, EUREC^{4}A [data set], https://howto.eurec4a.eu/botany_dales.html (last access: 18 June 2025), 2023b.

Jeevanjee, N. and Romps, D. M.: Convective self-aggregation, cold pools, and domain size, Geophys. Res. Lett., 40, 994–998, https://doi.org/10.1002/grl.50204, 2013.

Kazil, J., Vogel, R., Hamburg, U., Alinaghi, P., Antary, N., Bariteau, L., Bayley, C., Blossey, P., Boeing, S., Chandrakar, K. K., Dauhut, T., Denby, L., Ekman, A., Falk, N., Fridlind, A., Ghazaye, S., Heus, T., Hoffmann, F., Janssens, M., Jansson, F., Kang, L., Lim, J.-S., Mechem, D., Neggers, R., Raghunathan, G., Robbins, N., Savre, J., Schulz, H., Shima, S.-I., Siebesma, P., Tang, M., Tobias, N., Torri, G., van den Heever, S., Yamaguchi, T., Yanase, T., and Zuidema, P.: Cold Pool Analysis from The Cold Pool Model Intercomparison Project (CP-MIP), in: 105th AMS Annual Meeting, New Orleans, Louisiana, USA, 12–16 January 2025, AMS, 448635, 2025.

Lacis, A. A. and Hansen, J.: A parameterization for the absorption of solar radiation in the earth's atmosphere, J. Atmos. Sci., 31, 118–133, 1974.

Langhans, W. and Romps, D. M.: The origin of water vapor rings in tropical oceanic cold pools, Geophys. Res. Lett., 42, 7825–7834, https://doi.org/10.1002/2015GL065623, 2015.

Li, Z., Zuidema, P., and Zhu, P.: Simulated convective invigoration processes at trade wind cumulus cold pool boundaries, J. Atmos. Sci., 71, 2823–2841, https://doi.org/10.1175/JAS-D-13-0184.1, 2014.

Li, Z., Zuidema, P., Zhu, P., and Morrison, H.: The sensitivity of simulated shallow cumulus convection and cold pools to microphysics, J. Atmos. Sci., 72, 3340–3355, 2015.

Lochbihler, K., Lenderink, G., and Siebesma, A. P.: Cold pool dynamics shape the response of extreme rainfall events to climate change, J. Adv. Model. Earth Sy., 13, e2020MS002306, https://doi.org/10.1029/2020MS002306, 2021.

Matplotlib: Matplotlib, GitHub [code], https://github.com/matplotlib/matplotlib (last access: 15 March 2025), 2025.

McKinney, W.: Data Structures for Statistical Computing in Python, in: Proceedings of the 9th Python in Science Conference, Austin, Texas, USA, 28 June–3 July 2010, edited by: van der Walt, S. and Millman, J., 56–61, https://doi.org/10.25080/Majora-92bf1922-00a, 2010.

Myers, T. A., Scott, R. C., Zelinka, M. D., Klein, S. A., Norris, J. R., and Caldwell, P. M.: Observational constraints on low cloud feedback reduce uncertainty of climate sensitivity, Nat. Clim. Change, 11, 501–507, https://doi.org/10.1038/s41558-021-01039-0, 2021.

Narenpitak, P., Kazil, J., Yamaguchi, T., Quinn, P., and Feingold, G.: From sugar to flowers: A transition of shallow cumulus organization during ATOMIC, J. Adv. Model. Earth Sy., 13, e2021MS002619, https://doi.org/10.1029/2021MS002619, 2021.

Nissen, S. B. and Haerter, J. O.: Circling in on convective self-aggregation, J. Geophys. Res.-Atmos., 126, e2021JD035331, https://doi.org/10.1029/2021JD035331, 2021.

Nuijens, L. and Siebesma, A. P.: Boundary layer clouds and convection over subtropical oceans in our current and in a warmer climate, Current Climate Change Reports, 5, 80–94, 2019.

Nuijens, L., Stevens, B., and Siebesma, A. P.: The environment of precipitating shallow cumulus convection, J. Atmos. Sci., 66, 1962–1979, 2009.

NumPy: NumPy, GitHub [code], https://github.com/numpy/numpy (last access: 15 March 2025), 2025.

pandas: pandas, GitHub [code], https://github.com/pandas-dev/pandas (last access: 15 March 2025), 2025.

Quinn, P. K., Thompson, E. J., Coffman, D. J., Baidar, S., Bariteau, L., Bates, T. S., Bigorre, S., Brewer, A., de Boer, G., de Szoeke, S. P., Drushka, K., Foltz, G. R., Intrieri, J., Iyer, S., Fairall, C. W., Gaston, C. J., Jansen, F., Johnson, J. E., Krüger, O. O., Marchbanks, R. D., Moran, K. P., Noone, D., Pezoa, S., Pincus, R., Plueddemann, A. J., Pöhlker, M. L., Pöschl, U., Quinones Melendez, E., Royer, H. M., Szczodrak, M., Thomson, J., Upchurch, L. M., Zhang, C., Zhang, D., and Zuidema, P.: Measurements from the RV *Ronald H. Brown* and related platforms as part of the Atlantic Tradewind Ocean-Atmosphere Mesoscale Interaction Campaign (ATOMIC), Earth Syst. Sci. Data, 13, 1759–1790, https://doi.org/10.5194/essd-13-1759-2021, 2021.

Radtke, J., Naumann, A. K., Hagen, M., and Ament, F.: Therelationship between precipitation and its spatialpattern in the trades observed during EUREC4, Q. J. Roy. Meteor. Soc., 148, 1913–1928, 2022.

Radtke, J., Vogel, R., Ament, F., and Naumann, A. K.: Spatial organisation affects the pathway to precipitation in simulated trade-wind convection, Geophys. Res. Lett., 50, e2023GL103579, https://doi.org/10.1029/2023GL103579, 2023.

Rochetin, N., Hohenegger, C., Touzé-Peiffer, L., and Villefranque, N.: A Physically Based Definition of Convectively Generated Density Currents: Detection and Characterization in Convection-Permitting Simulations, J. Adv. Model. Earth Sy., 13, e2020MS002402, https://doi.org/10.1029/2020MS002402, 2021.

Rotunno, R., Klemp, J. B., and Weisman, M. L.: A theory for strong, long-lived squall lines, J. Atmos. Sci., 45, 463–485, https://doi.org/10.1175/1520-0469(1988)045<0463:ATFSLL>2.0.CO;2, 1988.

Savic-Jovcic, V. and Stevens, B.: The Structure and Mesoscale Organization of Precipitating Stratocumulus, J. Atmos. Sci., 65, 1587–1605, https://doi.org/10.1175/2007JAS2456.1, 2008.

Schlemmer, L. and Hohenegger, C.: The formation of wider and deeper clouds as a result of cold-pool dynamics, J. Atmos. Sci., 71, 2842–2858, https://doi.org/10.1175/JAS-D-13-0170.1, 2014.

Schneider, T., Teixeira, J., Bretherton, C. S., Brient, F., Pressel, K. G., Schär, C., and Siebesma, A. P.: Climate goals and computing the future of clouds, Nat. Clim. Change, 7, 3–5, 2017.

SciPy: SciPy, GitHub [code], https://github.com/scipy/scipy (last access: 15 March 2025), 2025.

Seabold, S. and Perktold, J.: statsmodels: Econometric and statistical modeling with python, in: 9th Python in Science Conference, Austin, Texas, 28 June–3 July 2010, https://doi.org/10.25080/Majora-92bf1922-011, 2010.

Seaborn: seaborn, GitHub [code], https://github.com/mwaskom/seaborn (last access: 15 March 2025), 2025.

Seifert, A. and Beheng, K. D.: A double-moment parameterization for simulating autoconversion, accretion and selfcollection, Atmos. Res., 59, 265–281, 2001.

Seifert, A. and Heus, T.: Large-eddy simulation of organized precipitating trade wind cumulus clouds, Atmos. Chem. Phys., 13, 5631–5645, https://doi.org/10.5194/acp-13-5631-2013, 2013.

Seifert, A., Heus, T., Pincus, R., and Stevens, B.: Large-eddy simulation of the transient and near-equilibrium behavior of precipitating shallow convection, J. Adv. Model. Earth Sy., 7, 1918–1937, 2015.

Snodgrass, E. R., Girolamo, L. D., and Rauber, R. M.: Precipitation Characteristics of Trade Wind Clouds during RICO Derived from Radar, Satellite, and Aircraft Measurements, J. Appl. Meteorol. Clim., 48, 464–483, https://doi.org/10.1175/2008JAMC1946.1, 2009.

Statsmodels: statsmodels, GitHub [code], https://github.com/statsmodels/statsmodels (last access: 15 March 2025), 2025.

Stensrud, D. J., Coniglio, M. C., Davies-Jones, R. P., and Evans, J. S.: Comments on "'A theory for strong long-lived squall lines' revisited", J. Atmos. Sci., 62, 2989–2996, https://doi.org/10.1175/JAS3514.1, 2005.

Stephens, G. L., Li, J., Wild, M., Clayson, C. A., Loeb, N., Kato, S., L'ecuyer, T., Stackhouse Jr., P. W., Lebsock, M., and Andrews, T.: An update on Earth's energy balance in light of the latest global observations, Nat. Geosci., 5, 691–696, 2012.

Stevens, B. and Feingold, G.: Untangling aerosol effects on clouds and precipitation in a buffered system, Nature, 461, 607–613, 2009.

Stevens, B., Bony, S., Farrell, D., Ament, F., Blyth, A., Fairall, C., Karstensen, J., Quinn, P. K., Speich, S., Acquistapace, C., Aemisegger, F., Albright, A. L., Bellenger, H., Bodenschatz, E., Caesar, K.-A., Chewitt-Lucas, R., de Boer, G., Delanoë, J., Denby, L., Ewald, F., Fildier, B., Forde, M., George, G., Gross, S., Hagen, M., Hausold, A., Heywood, K. J., Hirsch, L., Jacob, M., Jansen, F., Kinne, S., Klocke, D., Kölling, T., Konow, H., Lothon, M., Mohr, W., Naumann, A. K., Nuijens, L., Olivier, L., Pincus, R., Pöhlker, M., Reverdin, G., Roberts, G., Schnitt, S., Schulz, H., Siebesma, A. P., Stephan, C. C., Sullivan, P., Touzé-Peiffer, L., Vial, J., Vogel, R., Zuidema, P., Alexander, N., Alves, L., Arixi, S., Asmath, H., Bagheri, G., Baier, K., Bailey, A., Baranowski, D., Baron, A., Barrau, S., Barrett, P. A., Batier, F., Behrendt, A., Bendinger, A., Beucher, F., Bigorre, S., Blades, E., Blossey, P., Bock, O., Böing, S., Bosser, P., Bourras, D., Bouruet-Aubertot, P., Bower, K., Branellec, P., Branger, H., Brennek, M., Brewer, A., Brilouet, P.-E., Brügmann, B., Buehler, S. A., Burke, E., Burton, R., Calmer, R., Canonici, J.-C., Carton, X., Cato Jr., G., Charles, J. A., Chazette, P., Chen, Y., Chilinski, M. T., Choularton, T., Chuang, P., Clarke, S., Coe, H., Cornet, C., Coutris, P., Couvreux, F., Crewell, S., Cronin, T., Cui, Z., Cuypers, Y., Daley, A., Damerell, G. M., Dauhut, T., Deneke, H., Desbios, J.-P., Dörner, S., Donner, S., Douet, V., Drushka, K., Dütsch, M., Ehrlich, A., Emanuel, K., Emmanouilidis, A., Etienne, J.-C., Etienne-Leblanc, S., Faure, G., Feingold, G., Ferrero, L., Fix, A., Flamant, C., Flatau, P. J., Foltz, G. R., Forster, L., Furtuna, I., Gadian, A., Galewsky, J., Gallagher, M., Gallimore, P., Gaston, C., Gentemann, C., Geyskens, N., Giez, A., Gollop, J., Gouirand, I., Gourbeyre, C., de Graaf, D., de Groot, G. E., Grosz, R., Güttler, J., Gutleben, M., Hall, K., Harris, G., Helfer, K. C., Henze, D., Herbert, C., Holanda, B., Ibanez-Landeta, A., Intrieri, J., Iyer, S., Julien, F., Kalesse, H., Kazil, J., Kellman, A., Kidane, A. T., Kirchner, U., Klingebiel, M., Körner, M., Kremper, L. A., Kretzschmar, J., Krüger, O., Kumala, W., Kurz, A., L'Hégaret, P., Labaste, M., Lachlan-Cope, T., Laing, A., Landschützer, P., Lang, T., Lange, D., Lange, I., Laplace, C., Lavik, G., Laxenaire, R., Le Bihan, C., Leandro, M., Lefevre, N., Lena, M., Lenschow, D., Li, Q., Lloyd, G., Los, S., Losi, N., Lovell, O., Luneau, C., Makuch, P., Malinowski, S., Manta, G., Marinou, E., Marsden, N., Masson, S., Maury, N., Mayer, B., Mayers-Als, M., Mazel, C., McGeary, W., McWilliams, J. C., Mech, M., Mehlmann, M., Meroni, A. N., Mieslinger, T., Minikin, A., Minnett, P., Möller, G., Morfa Avalos, Y., Muller, C., Musat, I., Napoli, A., Neuberger, A., Noisel, C., Noone, D., Nordsiek, F., Nowak, J. L., Oswald, L., Parker, D. J., Peck, C., Person, R., Philippi, M., Plueddemann, A., Pöhlker, C., Pörtge, V., Pöschl, U., Pologne, L., Posyniak, M., Prange, M., Quiñones Meléndez, E., Radtke, J., Ramage, K., Reimann, J., Renault, L., Reus, K., Reyes, A., Ribbe, J., Ringel, M., Ritschel, M., Rocha, C. B., Rochetin, N., Röttenbacher, J., Rollo, C., Royer, H., Sadoulet, P., Saffin, L., Sandiford, S., Sandu, I., Schäfer, M., Schemann, V., Schirmacher, I., Schlenczek, O., Schmidt, J., Schröder, M., Schwarzenboeck, A., Sealy, A., Senff, C. J., Serikov, I., Shohan, S., Siddle, E., Smirnov, A., Späth, F., Spooner, B., Stolla, M. K., Szkółka, W., de Szoeke, S. P., Tarot, S., Tetoni, E., Thompson, E., Thomson, J., Tomassini, L., Totems, J., Ubele, A. A., Villiger, L., von Arx, J., Wagner, T., Walther, A., Webber, B., Wendisch, M., Whitehall, S., Wiltshire, A., Wing, A. A., Wirth, M., Wiskandt, J., Wolf, K., Worbes, L., Wright, E., Wulfmeyer, V., Young, S., Zhang, C., Zhang, D., Ziemen, F., Zinner, T., and Zöger, M.: EUREC^{4}A, Earth Syst. Sci. Data, 13, 4067–4119, https://doi.org/10.5194/essd-13-4067-2021, 2021.

Torri, G. and Kuang, Z.: On cold pool collisions in tropical boundary layers, Geophys. Res. Lett., 46, 399–407, https://doi.org/10.1029/2018GL080501, 2019.

Torri, G., Kuang, Z., and Tian, Y.: Mechanisms for convection triggering by cold pools, Geophys. Res. Lett., 42, 1943–1950, https://doi.org/10.1002/2015GL063227, 2015.

Touzé-Peiffer, L., Vogel, R., and Rochetin, N.: Cold pools observed during EUREC 4A: Detection and characterization from atmospheric soundings, J. Appl. Meteorol. Clim., 61, 593–610, 2022.

Twomey, S.: The Influence of Pollution on the Shortwave Albedo of Clouds, J. Atmos. Sci., 34, 1149–1152, https://doi.org/10.1175/1520-0469(1977)034<1149:TIOPOT>2.0.CO;2, 1977.

Vial, J., Vogel, R., and Schulz, H.: On the daily cycle of mesoscale cloud organization in the winter trades, Q. J. Roy. Meteor. Soc., 147, 2850–2873, https://doi.org/10.1002/qj.4103, 2021.

Virtanen, P., Gommers, R., Oliphant, T. E., Haberland, M., Reddy, T., Cournapeau, D., Burovski, E., Peterson, P., Weckesser, W., Bright, J., van der Walt, S. J., Brett, M., Wilson, J., Millman, K. J., Mayorov, N., Nelson, A. R. J., Jones, E., Kern, R., Larson, E., Carey, C. J., Polat, İ., Feng, Y., Moore, E. W., VanderPlas, J., Laxalde, D., Perktold, J., Cimrman, R., Henriksen, I., Quintero, E. A., Harris, C. R., Archibald, A. M., Ribeiro, A. H., Pedregosa, F., van Mulbregt, P., and SciPy 1.0 Contributors: SciPy 1.0: Fundamental Algorithms for Scientific Computing in Python, Nat. Methods, 17, 261–272, https://doi.org/10.1038/s41592-019-0686-2, 2020.

Vogel, R., Nuijens, L., and Stevens, B.: The role of precipitation and spatial organization in the response of trade-wind clouds to warming, J. Adv. Model. Earth Sy., 8, 843–862, https://doi.org/10.1002/2015MS000568, 2016.

Vogel, R., Konow, H., Schulz, H., and Zuidema, P.: A climatology of trade-wind cumulus cold pools and their link to mesoscale cloud organization, Atmos. Chem. Phys., 21, 16609–16630, https://doi.org/10.5194/acp-21-16609-2021, 2021.

Vogel, R., Albright, A. L., Vial, J., George, G., Stevens, B., and Bony, S.: Strong cloud–circulation coupling explains weak trade cumulus feedback, Nature, 612, 696–700, 2022.

Waskom, M. L.: seaborn: statistical data visualization, Journal of Open Source Software, 6, 3021, https://doi.org/10.21105/joss.03021, 2021.

Weisman, M. L. and Rotunno, R.: "A theory for strong long-lived squall lines" revisited, J. Atmos. Sci., 61, 361–382, https://doi.org/10.1175/1520-0469(2004)061<0361:ATFSLS>2.0.CO;2, 2004.

Xarray: Xarray, GitHub [code], https://github.com/pydata/xarray (last access: 15 March 2025), 2025.

Xie, Y. and Liu, Y.: A new approach for simultaneously retrieving cloud albedo and cloud fraction from surface-based shortwave radiation measurements, Environ. Res. Lett., 8, 044023, https://doi.org/10.1088/1748-9326/8/4/044023, 2013.

Xue, H., Feingold, G., and Stevens, B.: Aerosol effects on clouds, precipitation, and the organization of shallow cumulus convection, J. Atmos. Sci., 65, 392–406, https://doi.org/10.1175/2007JAS2428.1, 2008.

Yamaguchi, T., Feingold, G., and Kazil, J.: Cloud_phys: 2019 – Dataset for large-eddy simulation experiments related to the paper "Aerosol-cloud interactions in trade wind cumulus clouds and the role of vertical wind shear", NOAA Chemical Sciences Laboratory (CSL) [data set], https://csl.noaa.gov/groups/csl9/datasets/data/cloud_phys/2019-Yamaguchi-Feingold-Kazil/ (last access: 18 June 2025), 2019a.

Yamaguchi, T., Feingold, G., and Kazil, J.: Aerosol-cloud interactions in trade wind cumulus clouds and the role of vertical wind shear, J. Geophys. Res.-Atmos., 124, 12244–12261, 2019b.

Zhang, Y., Stevens, B., and Ghil, M.: On the diurnal cycle and susceptibility to aerosol concentration in a stratocumulus-topped mixed layer, Q. J. Roy. Meteor. Soc., 131, 1567–1583, https://doi.org/10.1256/qj.04.103, 2005.

Zuidema, P., Xue, H., and Feingold, G.: Shortwave radiative impacts from aerosol effects on marine shallow cumuli, J. Atmos. Sci., 65, 1979–1990, https://doi.org/10.1175/2007JAS2447.1, 2008.

Zuidema, P., Li, Z., Hill, R. J., Bariteau, L., Rilling, B., Fairall, C., Brewer, W. A., Albrecht, B., and Hare, J.: On trade wind cumulus cold pools, J. Atmos. Sci., 69, 258–280, https://doi.org/10.1175/JAS-D-11-0143.1, 2012.

Zuidema, P., Torri, G., Muller, C., and Chandra, A.: A survey of precipitation-induced atmospheric cold pools over oceans and their interactions with the larger-scale environment, Surv. Geophys., 38, 1283–1305, https://doi.org/10.1007/s10712-017-9447-x, 2017.